HIGH-TEMPERATURE CORROSION BEHAVIOR OF COATINGS AND ODS ALLOYS BASED ON Fe_3Al

P. F. Tortorelli, B. A. Pint, and I. G. Wright

Oak Ridge National Laboratory
Oak Ridge, Tennessee, U. S. A.

ABSTRACT

Iron-aluminide coatings were prepared by gas tungsten arc and gas metal arc weld-overlay techniques. All the weld overlays showed good oxidation/sulfidation behavior under isothermal conditions, including a gas metal arc deposit with only 21 at.% Al. A rapid degradation in corrosion resistance was observed under thermal cycling conditions when the initially grown scales spalled and the subsequent rate of reaction was not controlled by the formation of slowly growing aluminum oxides. Higher starting aluminum concentrations (>~25 at.%) are needed to assure adequate oxidation/sulfidation lifetimes of the weld overlays. A variety of stable oxides was added to a base Fe-28 at.% Al-2 % Cr alloy to assess the effect of these dopants on the oxidation behavior at 1200°C. A Y_2O_3 dispersion improved the scale adhesion relative to a Zr alloy addition, but wasn't as effective as it is in other alumina-forming alloys. Preliminary data for powder-processed Fe-28 at.% Al-2% Cr exposed to the H_2S-H_2-H_2O-Ar gas at 800°C showed that the oxidation/sulfidation rate was similar to that of many Fe_3Al alloys produced by ingot metallurgy routes.

INTRODUCTION

Iron aluminides containing greater than about 20-25 at.% Al have oxidation/sulfidation resistance at temperatures well above those at which these alloys have adequate mechanical strength.[1] In addition to alloying and processing modifications for improved creep resistance of wrought material, this strength limitation is being addressed by development of oxide-dispersion-strengthened (ODS) iron aluminides[2] and by evaluation of Fe_3Al alloy compositions as coatings or claddings on higher-strength, less corrosion-resistant materials.[3,4] As part of these efforts, the high-temperature corrosion behavior of iron-aluminide weld overlays and ODS alloys is being characterized and compared to previous results for ingot-processed material.

OXIDATION-SULFIDATION OF IRON-ALUMINIDE WELD OVERLAYS AT 800°C

This section contains corrosion data on weld deposits produced by the gas tungsten arc (GTA) process and initial observations of the oxidation/sulfidation behavior of a weld overlay synthesized by gas metal arc (GMA) welding. The development efforts associated with the GTA and GMA processes used to produce the weld overlays are described elsewhere.[3,5]

Rectangular specimens, approximately 18-25 mm x 12 mm, were cut from the weld overlay pads. As in previous oxidation-sulfidation studies,[6,7] coupons were then prepared by grinding away the substrate material so that only weld metal (approximately 1-2 mm thick) remained. Corrosion behavior was characterized by use of a continuous-recording microbalance to measure the weight of these specimens during exposure at 800°C to a flowing (~2 cm^3/s) mixed gas consisting of 5.4% H_2S-79.4% H_2-1.6% H_2O-13.6% Ar (by volume). The oxygen partial pressure, as determined by a solid-state oxygen cell, was 10^{-22} atm, and the sulfur pressure was calculated to be 10^{-6} atm. These types of exposures have been used to characterize the sulfidation resistance of iron aluminides and several other alloys.[6-9] In most cases, a specimen was held in the mixed-gas microbalance system at 800°C for a fixed amount of time, cooled to room temperature, and then removed from the system for subsequent examination. However, two specimens underwent thermal cycling, in which they experienced intermediate cooling to below 100°C and more than one hold period at the exposure temperature.

The use of welding to produce iron-aluminide coatings results in a loss of selected elements by vaporization and significant mixing of the filler metal and substrate alloys (dilution) during deposition. The final concentrations of the various elements in the weld deposit will depend on the particular filler metal/substrate combination and, therefore, the actual concentrations of the critical elements were determined using samples taken from the same welded plate as used to make the respective corrosion coupons (Table 1). Because there is essentially no aluminum in the substrates, the concentration of this element in the overlay will be significantly less than that of the weld rod/wire used to produce it. The extent of this dilution in aluminum depends on vaporization losses during welding and the relative amount of substrate material melted and thus is affected by parameters such as current, voltage, polarity, travel speed, etc. Similar dilution/enrichment considerations apply to the other elements. The composition of the weld overlays shown in Table I are consistent with the general dilution/enrichment factors found previously.[3,5-7]

Figure 1 shows the isothermal gravimetric results for corrosion specimens cut from the weld deposits listed in Table 1 and exposed to the H_2S-H_2-H_2O-Ar environment for 70-120 h at 800°C. While all the specimens showed relatively low-to-moderate weight gains, there were

Table 1. Weld Deposit Compositions

Weld Deposit	Process	Sub-strate	Concentration (at.%)[a] Al	Cr	Nb	Si	Ni	Mo	Zr	C
H1	GTA	304L	30.4	9.0	0.1	0.3	2.5	0.1	0.2	0.08
H2	GTA	Cr-Mo	37.3	6.2	<0.01	0.1	0.2	0.3	0.1	0.1
S1	GMA	Cr-Mo	21.3	6.0	<0.01	0.1	0.1	0.4	0.2	0.1

[a] Determined by spark source mass spectrometry. Balance is Fe.

distinct differences in their gravimetric behavior. These differences were also apparent visually. The surfaces of the specimen which exhibited the greatest sulfidation rate (H1) were almost completely covered with a dark corrosion product, while those of the H2 coupon showed a thin gray scale. The specimen cut from the S1 weld deposit exhibited a weight gain intermediate between H1 and H2 and developed a gray scale over most of its surface area with only some dark corrosion products along one edge. Some spallation of the scales formed on the H1 and S1 specimens occurred during cooling from the exposure temperature. Despite the differences in gravimetric behavior among the various weld overlays, each deposit composition showed substantially better isothermal oxidation/sulfidation resistance than that of conventional Fe-Cr-Ni and Fe-Cr-Al alloys.[8]

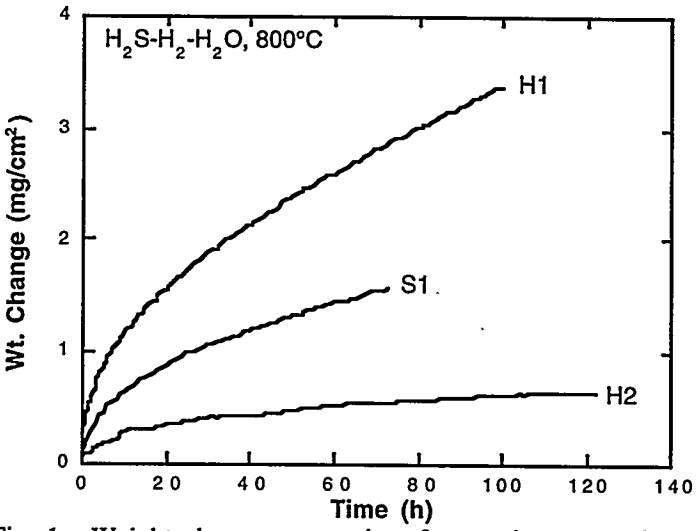

Fig. 1. Weight change versus time for specimens cut from iron-aluminide weld overlays and isothermally exposed to H_2S-H_2-H_2O-Ar at 800°C. The compositions of the weld overlays are shown in Table I.

Two more specimens of the S1 weld deposit were individually exposed in the microbalance system and held isothermally at 800°C in the mixed gas for about 72-74 h, after which they were allowed to cool to below 100°C. As shown in Fig. 2, the measured weight gains of S1-2 and S1-3 over this time period matched those measured for the first S1 coupon discussed above (S1-1). After its temperature fell to about 35°C, S1-2 was reheated to 800°C for several more hours, then cooled and removed from the system. In

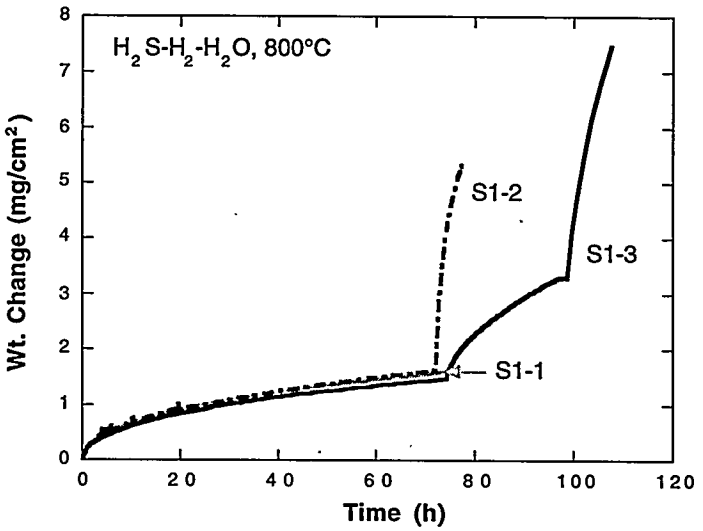

Fig. 2. Cumulative weight gain versus time for three individual specimens cut from weld-overlay S1 and then exposed to H_2S-H_2-H_2O-Ar at 800°C. The breaks in the curves represent reheating to exposure temperature after cooling to below 100°C. S1-1 was not reheated.

the case of S1-3, the coupon was cycled to below 100°C and back to the exposure temperature twice. For both of these specimens, significant increases in the rate of weight gain relative to the previous isothermal exposure periods were observed. Spallation occurred during the cooling cycles, but the data in Fig. 2 represent cumulative weight gains during the isothermal exposures and do not reflect any of this mass loss. At the end of the cyclic exposures, the specimen surfaces were covered with loosely adherent flakes of a dark corrosion product. Scanning electron microscopy (SEM) revealed a variety of product morphologies (Fig. 3); the platelets and needles resembled what has previously been identified as chromium and iron sulfides.[8,9] Subsequently, the loose scale was removed from the surfaces of the specimens. In both cases, it was combined with the material which had spalled during cooling or came off during handling to produce a powder that was analyzed by x-ray diffraction (XRD) and energy dispersive x-ray fluorescence (EDX). The corrosion products from S1-3 were a mixture of aluminum, iron, and chromium sulfides with a small amount (<1%) of oxide. Based on the most likely forms of these sulfides as determined by XRD, it appeared that the dominant ones were those incorporating aluminum (Al_2S_3) or iron (Fe_7S_8), with each composing about 45 - 48% of the total analyzed sample. For S1-2, Al_2O_3 was present in the scale in a greater concentration, in addition to iron, chromium, and chromium-iron sulfides. Little Al_2S_3 was detected. (It was not possible to determine the relative abundance of the various sulfides formed on S1-2 by EDX.)

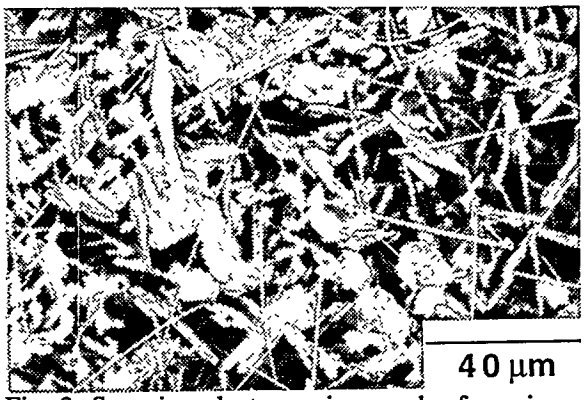

Fig. 3. Scanning electron micrograph of specimen S1-3 after three isothermal exposure periods in H_2S-H_2-H_2O-Ar at 800°C.

The excellent high-temperature corrosion resistance of bulk iron aluminides can be related to the rapid establishment and stability of a protective alumina scale and the absence or inhibited growth of iron and aluminum sulfides.[8] The inclusion of chromium in iron aluminides at levels greater than 2 - 3 at.% promotes more rapid reaction and increases weight gain due to the formation of chromium and iron sulfides.[8,9] On the other hand, little difference in isothermal gravimetric behavior was observed for variations in Al concentration (22-28% Al).[9] The isothermal weight gain behavior of the S1 specimen exactly matched that of Fe_3Al-5% Cr. Furthermore, the gravimetric data for the S1 composition were reproducible; three separate specimens cut from this weld deposit exhibited nearly identical weight changes over the equivalent isothermal time period (compare the first 72 h of exposure of S1-1, -2, and-3 in Fig. 2). However, these data are at variance with previous results from weld overlays:[6] a

coupon with the S1 composition (21% Al-6% Cr) would have been expected to have greater weight gains than those measured in the present study. Variations in minor alloying additions between the present and previous 21-23% Al weld overlays cannot explain the difference in gravimetric behavior; such elements were found to have minimal influence on overall oxidation/sulfidation resistance.[8] More likely, the discrepancy in results is probably due to higher than normal weight gains previously reported for weld overlays with lower aluminum levels[6] because of inadequate mixing during welding and/or rough initial surfaces that allowed localized regions to retain a composition like that of the substrate steel. In this sense, the GMA process, which involves a substantially higher energy input into the weld, may promote more complete mixing of the deposit and therefore result in more reproducible and better corrosion resistance at high temperatures.

As shown in Fig. 1, the S1 specimen (21.3% Al, 6% Cr) showed somewhat better isothermal oxidation/sulfidation behavior than the alloy containing 30% Al and 9% Cr (H1). This can again be explained on the basis of what is known from studies of the corrosion of bulk iron aluminides in this mixed gas. These studies[8,9] have shown that, under isothermal conditions, variations in chromium concentration have a greater effect on the corrosion behavior of Fe-(20-30%) Al alloys than changes in the aluminum concentration. Therefore, the higher weight gains for H1 (9% Cr) vis-à-vis S1 (6% Cr) are not unexpected. The H1 specimen showed a higher density of the black corrosion products associated with chromium (and iron) sulfides consistent with its higher chromium concentration.

The low rate of corrosion for the 37% Al composition (H2) agrees very well with previous results from weld overlays of similar composition.[6] Compared to gravimetric data for bulk Fe-28% Al-2% Cr and Fe-40% Al-6% Cr,[8] H2 showed a higher initial weight gain, but only a slightly greater longer-term corrosion rate. However, the high aluminum concentration of this deposit led to substantial cracking of the coating. While chemically resistant to this environment, the flaws in this weld overlay would have allowed the corrosive species access to the more susceptible substrate.

As described above, previous results from surface analysis of products formed on bulk iron aluminides and weld overlays revealed that Al_2O_3 and, under certain conditions, Al_2S_3 are predominant corrosion products when there is a higher aluminum content in the alloy, but faster growing sulfides of iron and chromium can form at lower concentrations of this element ($<$ 18-22% Al).[6,8,9] These considerations are important in understanding why the specimens of the S1 weld overlay composition (21% Al, 6% Cr) showed low oxidation/sulfidation rates under isothermal conditions, but suffered substantial degradation when subjected to thermal cycling (Figs. 2 and 3). Results from cyclic exposures of bulk iron aluminides (28% Al, $\leq$ 2%

Cr) in this mixed-gas environment showed that, despite some spallation of the corrosion products, the subsequent corrosion rate of alloys upon re-exposure was about the same as that measured initially.[8,9] For these aluminides, Al_2O_3 was able to reform following cooling and re-exposure, but this does not appear to be the case for the S1 weld overlay, where iron and chromium sulfides subsequently form at the expense of aluminum-containing products after a thermal cycle. The XRD and EDX data and SEM observations (Fig. 3) showed that, while Al_2O_3 appeared to be present initially, a substantial fraction of the corrosion products formed after two and three cycles (S1-2 and S1-3, respectively) were iron, chromium, and chromium-iron sulfides. The formation of these products are associated with the steep increases in weight gain with time shown in Fig. 2. This difference in thermal cycling behavior can be attributed to the lower initial aluminum concentration of the S1 composition (21%) compared to the typical Fe_3Al alloys (28% Al). As mentioned above, the Al concentration of the S1 overlay is close to the critical concentration necessary for good sulfidation resistance of binary Fe-Al alloys.[9] Therefore, any decrease in aluminum level will lead to more rapid corrosion associated with predominant growth of iron and chromium sulfides. Such aluminum depletion can occur by formation of aluminum-containing corrosion products followed by spallation during cooling. Upon further exposure, there is insufficient aluminum remaining in the surface regions to maintain the preferential development of the more slowly growing aluminum-containing products, and a higher rate of weight gain is observed, as in the present case. Indeed, the rates of accelerated weight gain after the initial exposures (S1-2 and -3, Fig. 2) are similar to those measured for alloys that form scales preferentially composed of transition-metal sulfides.[8]

The present results indicate that the aluminum concentration of the S1 weld overlay (21.3%) appears to be sufficient to maintain corrosion resistance in an aggressive oxidizing/sulfidizing environment under isothermal conditions, but that a greater amount of aluminum is required in the deposit to assure acceptable corrosion behavior of such coatings under thermal cycling conditions. Higher concentrations would not only delay any onset of accelerated reaction caused by aluminum depletion but would also improve the corrosion behavior of iron aluminide coatings containing substrate elements that are deleterious to sulfidation resistance (such as chromium and nickel).[6] However, as noted previously, weld deposits containing high aluminum concentrations are very sensitive to hydrogen-induced cracking which would allow corrosion of the substrate by ingress of reactive species. Therefore, the development of iron-aluminide coatings must involve an optimization of the composition and welding parameters such that good corrosion and cracking resistance are attained.

OXIDATION AND OXIDATION-SULFIDATION OF ODS Fe_3Al ALLOYS

Powders of gas-atomized Fe-28% Al-2% Cr (FAS) and various submicron oxides were mechanically blended in a flowing Ar atmosphere using a high-speed attritor and stainless steel balls.[2,10] The blended powder was canned, degassed, and extruded at 1100°C. For comparison, a FAS powder extrusion without an oxide addition (FASN), ingot-processed Fe-28% Al-5% Cr-0.1% Zr (FAL), and a commercial ZrO_2-dispersed (0.06% Zr) Fe-20% Cr-10% Al alloy (Kanthal alloy APM) were also tested. Cyclic oxidation experiments were conducted at 1200°C in air using procedures described in ref. 2. Oxide additions were normally made at a standard 0.2 cation % level.

Initial oxidation evaluation used twenty 2-h cycles at 1200°C as a way to assess the performance of the different dopants. The weight change data are shown in Fig. 4. As a reference, Kanthal APM showed almost no spallation and had a weight change almost identical to that measured isothermally.[11] Oxide additions of Ce, La and Sc accelerated the oxidation rate and, in the case of CeO_2, led to FeO formation.[10] This detrimental influence has been observed for a number of oxide additions, such as CeO_2 in FeCrAl,[12] and can be an effect of over-doping. In order to test this explanation, smaller amounts of La_2O_3 (0.05%La) and CeO_2 (0.1%) were added to FAS. This approach reduced the negative effects, but did not eliminate them; during longer-term testing (10 x 100 h cycles, see Fig. 5), these alloys exhibited accelerated and breakaway oxidation.

The short-term cyclic oxidation behavior of FAS was similar regardless of whether the added dopant was an oxide of Y, Nd, Yb, Hf or Zr (Fig. 4). In each case, after an initial specimen weight gain, each subsequent cycle reuslted in monotonic decreases in weight signifying some spallation after each thermal cycle. As such, these results did not sufficiently differentiate the effects of the various dopants and longer-term cyclic exposures were required to examine the influence of

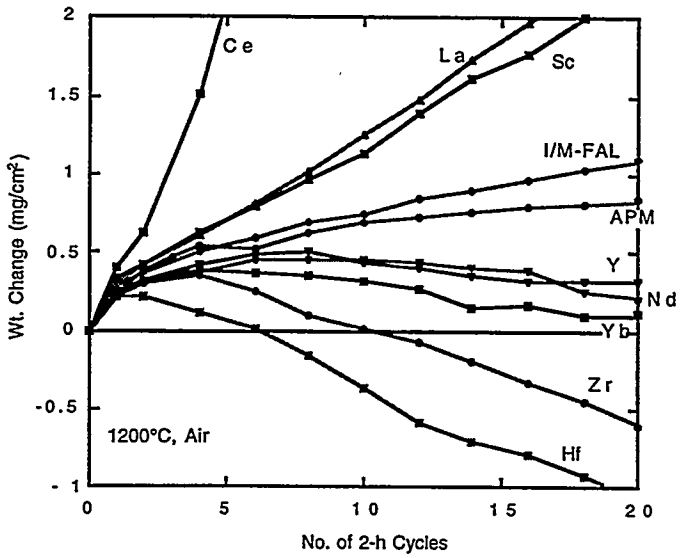

Fig. 4. Specimen weight change versus number of 2-h oxidation cycles of Fe - 28% Al - 2% Cr (FAS) with various cation oxide dispersions (0.2 at.%) in air at 1200°C.

different oxide additions on oxidation behavior. Data from these exposures showed that Y_2O_3-dispersed FAS performed better than any of the other iron-aluminide alloys (Fig. 5), including the ingot-processed alloy containing Zr (FAL), which has improved scale adhesion relative to other wrought iron aluminides.[13] Because there were only small differences in the parabolic rate constants of the various alloys,[14] the lower rate of weight gain of Y_2O_3-dispersed FAS reflected a reduced degree of scale spallation rather than an effect on scale growth kinetics. (More extensive cyclic oxidation results for Y_2O_3-dispersed FAS can be found in ref. 2.) The Hf, Nd, Yb and Zr additions did produce some beneficial effect compared to an Al_2O_3 dispersion (which is always present in the as-fabricated ODS FAS alloys); in long-term cyclic exposures, breakaway oxidation was observed for FAS doped only with Al_2O_3.[14]

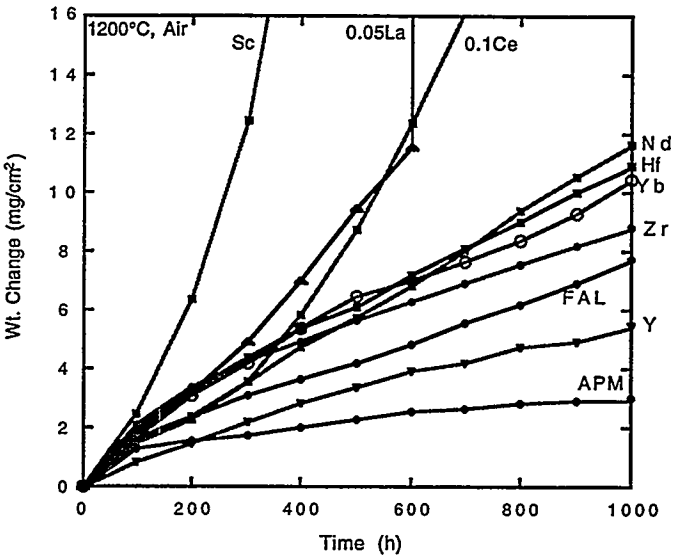

Fig. 5. Total weight change (specimen plus spalled scale) versus time for specimens cyclically oxidized in air at 1200°C (100-h cycles). Except where shown, all cation concentrations were 0.2%.

Although Y_2O_3 has a positive influence on the spallation resistance of FAS, the present results indicate that this dopant is not as effective in iron aluminides as when it is added to FeCrAl and β-NiAl.[14] Likewise, ZrO_2 in FAS did not replicate the effect of this dopant in commercial APM (Fig. 5). There are several possible reasons for the variations in a dopant's effectiveness, including alloy substrate strength and its effect on scale buckling and void formation.[14] Additionally, while 0.2% Y appeared to be an optimum doping level,[14] this may not be true for the other additions. For example, assuming that the APM alloy has an optimized ZrO_2 content of 0.06 at.% Zr, the 0.2% Zr addition used in this study may not produce the best effect that could be achieved. Lower (0.05%) dopant levels of Zr and Hf are currently being investigated.

As noted in the previous section, Fe_3Al alloys produced by conventional ingot metallurgy (I/M) procedures, and FAS in particular, have excellent sulfidation resistance in H_2S-containing environments.[8,9] Therefore, it is of interest to learn whether ODS iron aluminides show similar corrosion behavior. Preliminary data in this regard were obtained by exposing FASN and FAS-

Y_2O_3 (0.2 cation %) to H_2S-79.4% H_2-1.6% H_2O-13.6% Ar in similar experiments to those described above for the weld overlay specimens. The results are shown in Fig. 6, which also contains data for FAS, a Fe-28% Al-5% Cr-1% Nb-0.5% C iron aluminide, and a FeCrAl-type Fe- 18% Cr - 12% Al alloy produced by ingot processing (FAS-I/M, FA129-I/M, and Fe-18Cr-12Al-I/M, respectively). Note that the isothermal weight gains of the powder metallurgy-processed alloys were somewhat greater than the I/M FAS, but less than the Fe_3Al-5Cr alloy (FA129-I/M). Much of the difference in the weight gains was established in the early stages of exposure to the oxidizing/sulfidizing environment; at extended times the rates of weight gain are quite similar for the ingot- and powder-processed FAS alloys. The reason for the more rapid initial weight gains of the P/M alloys is not yet known, but it doesn't seem to be related to increases in the chromium levels during the milling process; the chromium concentrations in FASN and FAS-Y_2O_3 after extrusion were just 2.0 and 2.4%, respectively. Rather, the fine grain size of these as-extruded alloys (about 1 μm) may allow a more rapid diffusion of chromium to the reaction front[15] and result in higher weight gains due to formation of chromium sulfides. As noted above, the presence of chromium in Fe_3Al in excess of about 2% leads to higher corrosion rates in this mixed-gas environment. Nevertheless, these preliminary results for ODS Fe_3Al alloys indicate good overall sulfidation resistance. The weight gains for these materials are significantly less than for a FeCrAl-type alloy (Fig. 6) and are dramatically better than those measured for a stainless steel.[8]

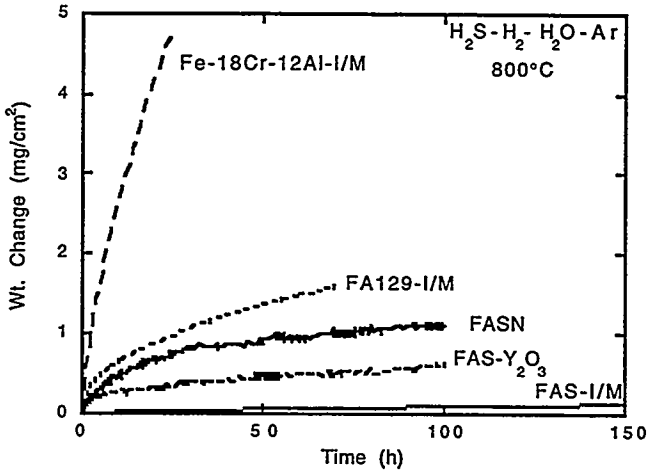

Fig. 6. Weight change versus time for specimens isothermally exposed to H_2S-H_2-H_2O-Ar at 800°C.

SUMMARY AND CONCLUSIONS

The high-temperature strength limitations of Fe_3Al alloys are being addressed by evaluation of these compositions as coatings or claddings on higher-strength, less corrosion-resistant materials and by development of oxide-dispersion-strengthened (ODS) iron aluminides with oxidation and sulfidation resistance that match or exceed that of ingot-produced versions of these materials. Iron-aluminide coatings were prepared by gas tungsten arc and gas metal arc

weld-overlay techniques. All the weld overlays showed good oxidation/sulfidation behavior under isothermal conditions, including a gas metal arc deposit with only 21 at.% Al. A rapid degradation in corrosion resistance was observed under thermal cycling conditions when the initially grown scales spalled and the subsequent rate of reaction was not controlled by the formation of slowly growing aluminum oxides. Higher starting aluminum concentrations (>~25 at.%) are needed to assure adequate oxidation/sulfidation lifetimes of the weld overlays. A variety of stable oxides was added to a base Fe-28 at.% Al-2 % Cr alloy to assess the effect of these dopants on the oxidation behavior at 1200 and 1300°C in air and O_2. A Y_2O_3 dispersion improved the scale adhesion relative to a Zr alloy addition, but wasn't as effective as it is in other alumina-forming alloys. Preliminary exposures of ODS Fe-28 at.% Al-2% Cr in the H_2S-H_2-H_2O-Ar gas at 800°C showed that the oxidation/sulfidation resistance of these alloys was good.

ACKNOWLEDGMENTS

The authors thank M. Howell for experimental support and J. R. DiStefano, G. M. Goodwin, and C. G. McKamey for their reviews of the manuscript. This research was sponsored by the Fossil Energy Advanced Research and Technology Development (AR&TD) Materials Program, U S. Department of Energy, under contract DE-AC05-96OR22464 with Lockheed Martin Energy Research Corporation. B. A. Pint is supported by the U. S. Department of Energy Distinguished Postdoctoral Research Program administered by the Oak Ridge Institute for Science and Education.

REFERENCES

1. C. G. McKamey, J. H. DeVan, P. F. Tortorelli, and V. K. Sikka, J. Mater. Res. 6 (1991) 1779-1805.

2. I. G. Wright, B. A. Pint, E. K. Ohriner, and P. F. Tortorelli, "ODS Iron Aluminides," these proceedings.

3. G. M. Goodwin, P. J. Maziasz, C. G. McKamey, J. H. DeVan, and V. K. Sikka, pp. 205-10 in *Proc. Eighth Annual Conf. Fossil Energy Materials*, N. C. Cole and R. R. Judkins (comp.), CONF-9405143, U. S. Department of Energy, August 1994.

4. K. Natesan, pp. 591-99 in Heat-Resistant Materials II, K. Natesan, P. Ganesan, and G. Lai (eds.), ASM International, August 1995.

5. G. M. Goodwin, "Weld Overlay Cladding with Iron Aluminides," these proceedings.

6. P. F. Tortorelli, J. H. DeVan, G. M. Goodwin, and M. Howell, pp. 203-12 in Elevated Temperature Coatings: Science and Technology I, N. B. Dahotre, J. M. Hampikian, and J. J. Stiglich (eds.), The Minerals, Metals, and Materials Society, Warrendale, PA, 1995.

7. P. F. Tortorelli, G. M. Goodwin, M. Howell, and J. H. DeVan, pp. 585-90 in Heat-Resistant Materials II, K. Natesan, P. Ganesan, and G. Lai (eds.), ASM International, August 1995.

8. J. H. DeVan, pp. 107-115 in Oxidation of High-Temperature Intermetallics, T. Grobstein and J. Doychak (eds.), The Minerals, Metals, and Materials Society, 1989.

9. J. H. DeVan and P. F. Tortorelli, Mater. at High Temp. 11 (1993) 30-35.

10. B. A. Pint, K. B. Alexander, and P. F. Tortorelli, pp. 1315-20 in High-Temperature Ordered Intermetallic Alloys VI, J. A. Horton, I. Baker, S. Hanada, R. D. Noebe, and D. S. Schwartz (eds.), The Materials Research Society, Pittsburgh, PA, 1995.

11. B. A. Pint, A. J. Garratt-Reed, and L. W. Hobbs, Mater. High. Temp. 13 (1995) 3.

12. B. A. Pint, "Study of the Reactive Element Effect in ODS Iron-Base Alumina-Formers," submitted for publication in Mater. Sci. Forum, March 1996.

13. P. F. Tortorelli and J. H. DeVan, pp. 257-70 in Processing, Properties, and Applications of Iron Aluminides, J. H. Schneibel and M. A. Crimp (eds.), The Minerals, Metals, and Materials Society, Warrendale, PA, 1994.

14. B. A. Pint, P. F. Tortorelli, and I. G. Wright, "The Oxidation Behavior of ODS Iron Aluminides," submitted for publication in Werst. Korros., March 1996.

15. G. J. Yurek, D. Eisen, and A. J. Garratt-Reed, Metall. Trans. A 13A (1982) 473-85.

EVALUATION OF THE INTRINSIC AND EXTRINSIC FRACTURE BEHAVIOR OF IRON ALUMINIDES

Bruce S. Kang[1], Qizhou Yao[2] and Bernard R. Cooper[3]

[1,2]Mechanical and Aerospace Engineering Department
[3]Physics Department
West Virginia University
Morgantown, WV 26506

ABSTRACT

Comparative creep crack growth tests of FA-186 and FA-187 iron aluminides under either dry oxygen or air environment showed that both alloys are susceptible to room temperature hydrogen embrittlement. Test results also revealed that FA-187 is intrinsically a more brittle material than FA-186. Atomistic computational modeling is being undertaken to find the preferred geometries, structures and formation energies of iron vacancies and vacancy pairs (Fe-Fe) in FeAl and Fe_3Al. An indication of vacancy clustering in Fe_3Al, with consequences for dislocation behavior, may be important for understanding the role of dislocation assisted diffusion in the hydrogen embrittlement mechanism.

INTRODUCTION

Because of their excellent corrosion resistance in high temperature oxidizing-sulfidizing environments in combination with low cost and other advantages, iron aluminides are of great potential use in fossil energy technology, however, there are problems at room and medium temperatures with hydrogen embrittlement as related to exposure to moisture.[1,2] In this research, a coordinated computational modeling/experimental study of mechanisms central to mechanical and fracture behavior in these materials from room to medium temperatures under either air or moisture-free environment is undertaken. Some preliminary results of our first year research effort are presented in this paper. The initial computational modeling is focused on the study of iron vacancy and divacancy behavior which may be important for understanding how dislocation assisted diffusion may enter the hydrogen embrittlement mechanism. A fully quantum mechanical full-potential LMTO technique, including force calculations, is being applied to find the preferred geometries, structures

and formation energies of iron vacancies and vacancy pairs (Fe-Fe) in FeAl and Fe_3Al. As for the experimental research, four iron aluminides with various alloy additives such as Zr, C, Nb, or B are selected to study the effect of alloy additives to fracture behavior, in particular, the improvement of resistance to hydrogen embrittlement. Four crack growth test results of iron aluminides (FA-186 and FA-187) subjected to constant tensile loading in air or dry oxygen environment are discussed in this paper. Moire interferometry is used to obtain full-field crack-tip deformations which will be used to determine crack tip plastic yield zone and fracture parameters such as J-integral or stress intensity factor. Post mortem fractography evaluation is also carried out to correlate the measured crack tip deformations to microstructural characteristics.

COMPUTATIONAL MODELING

The iron vacancy distribution is central to understanding mechanisms controlling the strength of iron aluminides generally, and may also play a key role in the mechanisms by which hydrogen penetrates and embrittles iron aluminides, such as dislocation-assisted diffusion.[2] For these reasons the initial focus in our computational modeling study of iron aluminides is on the tendency of iron vacancies to cluster. To investigate this question we are first looking at the energetics favoring the formation of a divacancy compared to the energy of two isolated vacancies. This calculation will include the effects of lattice relaxation. The method being used is our well established fully quantum mechanical full potential linear combination of muffin-tin-orbitals (LMTO) technique.[3,4] This is an ab initio all-electron technique with full relativistic corrections included. To assure high accuracy we have implemented an augmented basis through use of multiple κ's and energy windows.[4,5] Initially we have found the preferred unrelaxed geometry through use of total energy minimization. For FeAl this gives a formation energy of 4.6eV, and a calculated lattice constant of 2.82 Å and bulk modulus of 165.39 GPa. This value for the lattice constant compares favorably to the experimental value[6] of 2.90 Å and the value of 2.83 Å calculated earlier by Fu and Yoo[7]; while the bulk modulus compares to Fu and Yoo's calculated value of 187.84 GPa.

Our initial calculation of vacancy formation energy is for FeAl, prior to proceeding to the study of Fe_3Al, the system of greater practical interest. We find the unrelaxed formation energy of a single iron vacancy in FeAl is 1.0eV. This compares favorably to the experimental value[8] of 0.98±0.07eV and the value of 0.97eV calculated by Fu et al.[9] Judging from the behavior in aluminum,[10] we expect

relaxation effects to lower this by an amount of at most 0.1eV, which would correspond to the lower part of the experimental range. To treat relaxation effects for this transition metal system, we have implemented a force methodology based on our full-potential LMTO total energy technique and will apply this to vacancy and divacancy formation energies in both FeA*l* and Fe_3Al. As a test of this methodology, we have calculated the formation energy of a fully relaxed vacancy in aluminum and obtained a value of 0.56eV in comparison with the experimental value of 0.60-0.67eV and the value of 0.66±0.03eV calculated by Chetty et al [10] using a pseudopotential-based technique.

EXPERIMENTAL PROGRAM

Materials

Alloys used in this study were fabricated at Oak Ridge National Laboratory (ORNL) by vacuum induction melting and casting into graphite molds. The ingots were then hot forged (two passes, 25% per pass) at 1000°C followed by hot rolled at 800°C for seven passes (15% per pass) to produce finished plate thickness of 6.35 mm. The finished plates were either heat treated at 900°C for one hour then air quenched to produce partially ordered B2 structure or heat treated at 900°C for one hour followed by 550°C for 72 hours then air quenched to produce DO_3 structure. Four alloys (FA-186, FA-187, FA-188, and FA-189) were received, however, only test results of FA-186 and FA-187 are presented in this paper. Table 1 shows the alloy composition of FA-186 and FA-187.

Singe-edge-notched (SEN) specimens were cut from the plates using EDM machine and specimen surfaces were hand-polished with fine grid sandpapers. Figure 1 shows the test specimen geometry. The notch of each specimen was cut using 0.1 mm diameter EDM wire with notch direction parallel to the rolling direction.

Moire Interferometry

Moire interferometry was developed in the 1980's [11] and has been used to examine a variety of problems in composite materials, interface mechanics and fracture mechanics. Moire interferometry is capable of high sensitivity full-field surface deformation measurement (typical measurement sensitivity can range from 0.1 μm/fringe to 1.6 μm/fringe). Recently, we have demonstrated that moire interferometry can be applied to study environmental assisted cracking problems.[12,13] In this research, an environmental chamber was constructed to conduct crack growth tests of iron

aluminides under controlled gas content (air, argon, hydrogen gas or dry oxygen) environments. Figure 2 shows schematic drawing of the optical setup for moire interferometry test with the environmental chamber mounted on the optical bench.

RESULT AND DISCUSSION

Table 2 shows the test matrix. As shown in the table, four tests of FA-186 and FA-187 SEN specimens were conducted under constant tensile loading condition in either dry oxygen or air environment. Figures 3 to 6 shows typical recorded moire fringe patterns at different time intervals. Specimen 186#1 was tested in dry oxygen under initial applied K_I value of 25 MPa$\sqrt{m}$ for nineteen hours with little change of crack tip deformation fields (as shown in Fig. 3). At t = 1124 minutes, the applied K_I value was increased to 28.7 MPa$\sqrt{m}$ and we observed steady increase of crack tip damage zone (dark region), after 21 minutes (t = 1145 minutes), the specimen failed. As for specimen 186#2, it was tested in air with the same initial applied K_I value of 25 MPa$\sqrt{m}$. The recorded moire fringes showed slowly increased creep crack tip deformations (Fig. 4). We also observed the existence (pop-in) of secondary micro cracks at notch tip region right after the 25 MPa$\sqrt{m}$ K_I load was applied; these micro cracks may be caused by the stress-assisted localized crack tip hydrogen embrittlement. At t = 95 minutes, the applied K_I value was increased to 28.3 MPa$\sqrt{m}$ and quickly (within 20 seconds), the bottom portion of the micro cracks coalesced to trigger unstable crack propagation to failure. Figure 7 shows the corresponding SEM fractographs which indicated transgranular cleavage failure for both FA-186 specimens, however, the one tested in air had rougher cleavage facets (i.e. more tilt and twist boundaries). Since in hydrogen-free environment, cleavage generally takes place along crystallographic planes with the lowest packing density and thus resulted in larger cleavage facets. While in hydrogen-containing environment, hydrogen embrittlement is proposed to be associated with dislocation transport of hydrogen[2], which occurred along crystallographic planes with the highest packing density, i.e. more rougher cleavage facets for specimen 186#2.

As for the FA-187 specimens which contain small amount of Zr and C, the same initial loading condition (K_I = 25 MPa$\sqrt{m}$) was applied (see Table 2) and, as shown in Figs. 5 and 6, the one tested in dry oxygen lasted for about 18 minutes and the one tested in air lasted for only 2 minutes. For both specimens, initial steady crack extension was observed. Figure 8 shows representative

SEM fractographs in areas 1, 2 and 3. Based on the moire fringes, we observe that specimen 187#1 had slow crack extension from initial notch to the beginning portion of area 3 followed by unstable crack propagation, and specimen 187#2 had slow crack extension from initial notch up to the mid-section of area 2 followed by unstable fracture. From Fig. 8, it is noted that the slow crack extension of FA-187 SEN specimens is characterized by intergranular fracture. For specimen 187#2 tested in air, the effect of hydrogen embrittlement is evident and resulted in shorter crack extension and time duration. Our test results indicated the FA-187 is intrinsically more brittle than FA-186. As discussed in ref. 14, the level of zirconium addition needs to be carefully controlled; some amount of zirconium addition (say about 0.1%) is beneficial to promote scale adhesion for protection against corrosion in harsh environment, however, too much zirconium addition (such as 0.5% Zr in FA-187) may produce intrinsically brittle iron aluminide alloy.

CONCLUSION

Comparative creep crack growth tests of FA-186 and FA-187 SEN specimens under either dry oxygen or air environment showed substantial difference of crack-tip deformation profile and evidence of hydrogen embrittlement for both the FA-186 and FA-187 iron aluminides. Test results also revealed that FA-187 is intrinsically a more brittle material than FA-186.

Additional comparative tests are planned for FA-188 and FA-189 alloys. Evaluation of crack tip plastic yield zone (or damage zone) and fracture parameters such as J-integral or stress intensity factor based on the measured moire fringes is currently undertaken. Research collaboration with ORNL researchers on computational modeling and microstructural analysis should elucidate the intrinsic and extrinsic fracture behavior of the Fe-28Al-5Cr series iron aluminides.

ACKNOWLEDGMENT

This research is sponsored by the U.S. Department of Energy, Office of Fossil Energy, Advanced Research and Technology Development (AR&TD) Materials Program at the Oak Ridge National Laboratory under contract no. SUB-19X-ST547C with Lockheed Martin Energy Systems, Inc. Technical assistance of Dr. C.T. Liu at ORNL is gratefully acknowledged.

REFERENCES

1. N.S. Stoloff and C.T. Liu, "Environmental Embrittlement of Iron Aluminides - Review," Intermetallics, 2, pp.75-87, (1994).
2. A. Castagna, D.A. Alven and N.S. Stoloff, " Environmental Embrittlement of Iron Aluminides under Cyclic Loading Condition," Proceedings of the Ninth Annual Conference on Fossil Energy Materials, Oak Ridge, TN, pp. 377-386, May 16-18 (1995).
3. D.L. Price and B.R. Cooper, Phys. Rev. B 39, 4945 (1989).
4. D.L. Price, B.R. Cooper and J.M. Wills, Phys. Rev. B 46, 11, 368 (1992).
5. D.L. Price, J.M. Wills, and B.R. Cooper Phys. Rev. B 48, 15, 301 (1993).
6. M.H. Yoo, T. Takasugi, S. Hanada, and O. Izumi, Mater. Trans. Japan Inst. Metals 31, 435 (1990).
7. C.L. Fu and M.H. Yoo, Acta, Metall, Mater, 40, 703 (1992).
8. R. Wurschum, C. Grupp, and H.E. Schaefer, Phys. Rev. Lett, 75, 97 (1995).
9. C.L. Fu, Y.Y. Ye, M.H. Yoo, and K.M. Ho, Phys. Rev. B48, 6712 (1993).
10. N. Chetty, M. Weinert, T.s. Rahman, and J.W. Davenport, Phys. Rev. B 52, 6313 (1995).
11. D. Post, Moire interferometry, Chapter 7 in SEM, Handbook on Experimental Mechanics, ed. A.S. Kobayashi. Prentice-Hall, Englewood Cliffs, NJ, pp.314-387, (1987).
12. F.X. Wang and B.S.-J. Kang, Moire Interferometry in Liquid Medium, SEM, Proceeding of the VII International Congress on Experimental Mechanics, PP.1711-1716, Las Vegas, NA, June 8-11 (1992) .
13. B.S.-J. Kang, G. Zhang, P. Liu and M. Ellathur, Stress Accelerated Grain Boundary Oxygen Embrittlement on Creep Crack Growth of Ni-base Superalloys, 1995 ASME Winter Conference, San Francisco, CA, November, 20-24 (1995).
14. C.G. McKamey, P.J. Maziasz and Y. Marrero-Santos, Effects of Composition and Heat Treatment at 1150°C on Creep-Rupture Properties of Fe_3Al-based Alloys, Proceedings of the Ninth Annual Conference on Fossil Energy Materials, Oak Ridge, TN, pp. 369-376, May 16-18 (1995).

Table 1 Chemical Composition of Fe-Al Alloys (at%)

Composition	Fe	Al	Cr	Zr	C
FA - 186	balance	28	5		
FA - 187	balance	28	5	0.5	0.05

Table 2 Test Matrix

Specimen	a/W	Structure	Applied K (MPa√m)	Environment	Lasting Time
186 #1	0.65	DO_3	25 28.7	Dry Oxygen Dry Oxygen	19 hrs 21 min
186 #2	0.65	DO_3	25 28.3	Air Air	94 min 1 min
187 #1	0.4	DO_3	25	Dry Oxygen	18 min
187 #2	0.4	DO_3	25	Air	2 min

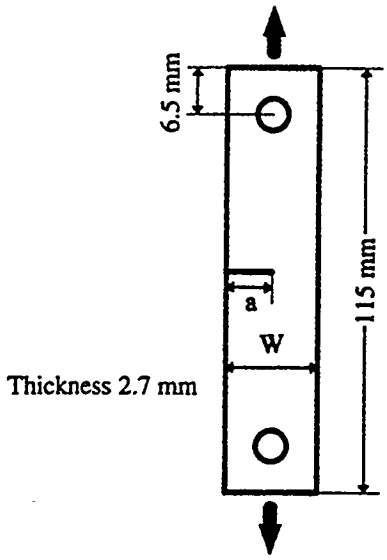

Fig. 1 Test specimen geometry.

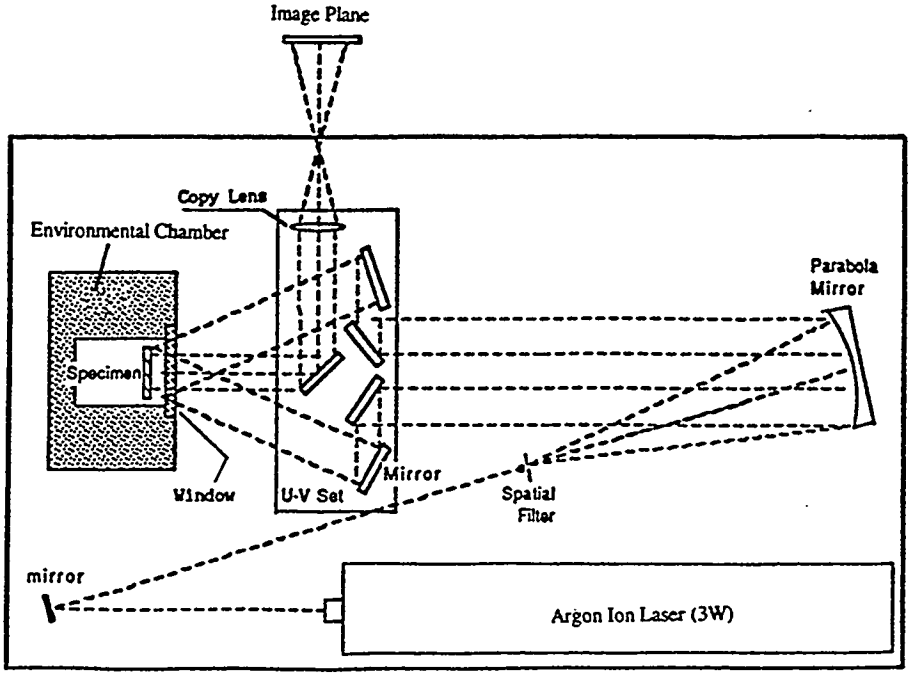

Fig. 2 Optical setup for moire interferometry test.

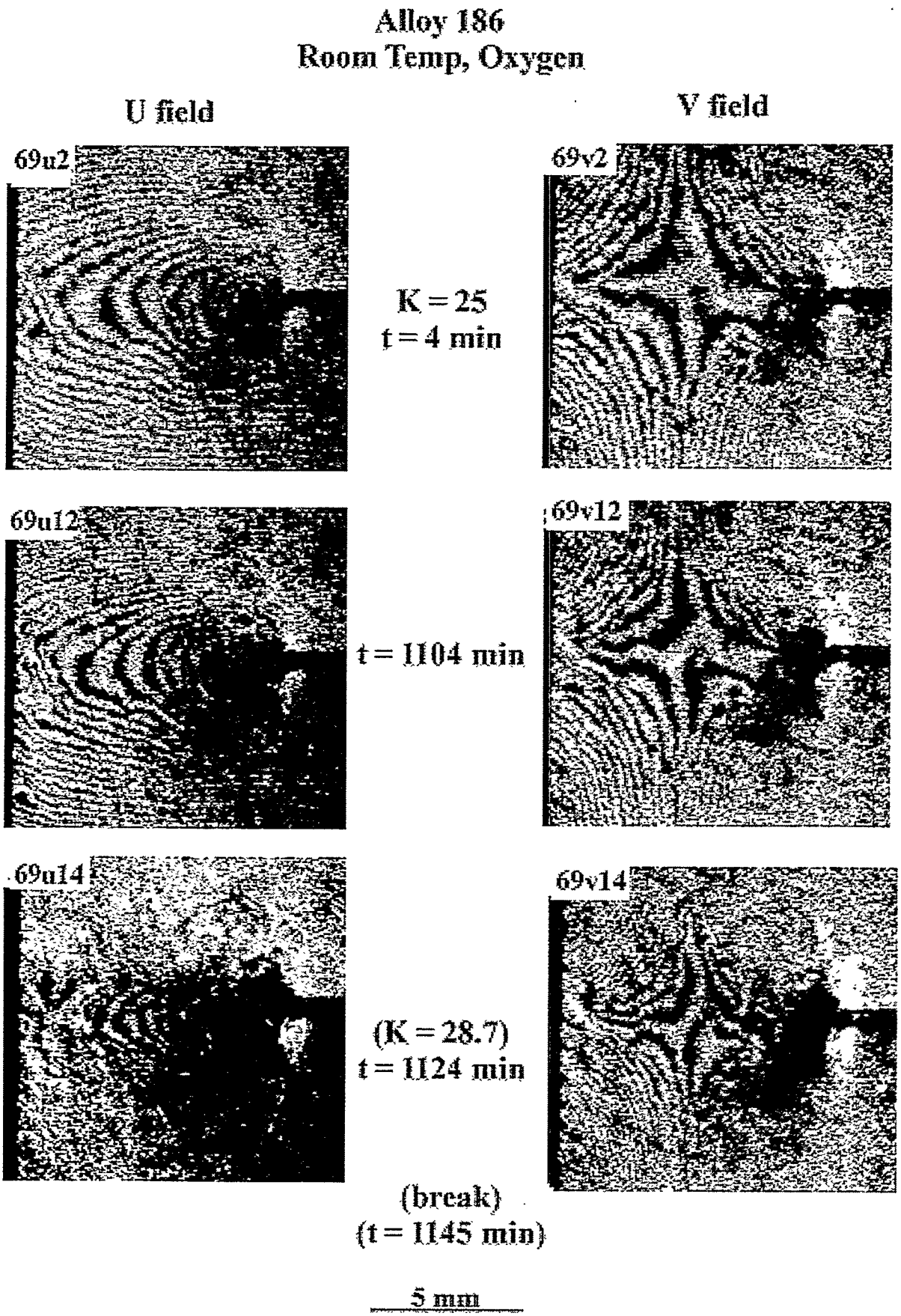

Fig. 3 U and V displacement fields of alloy FA-186 SEN specimen tested in dry oxygen.

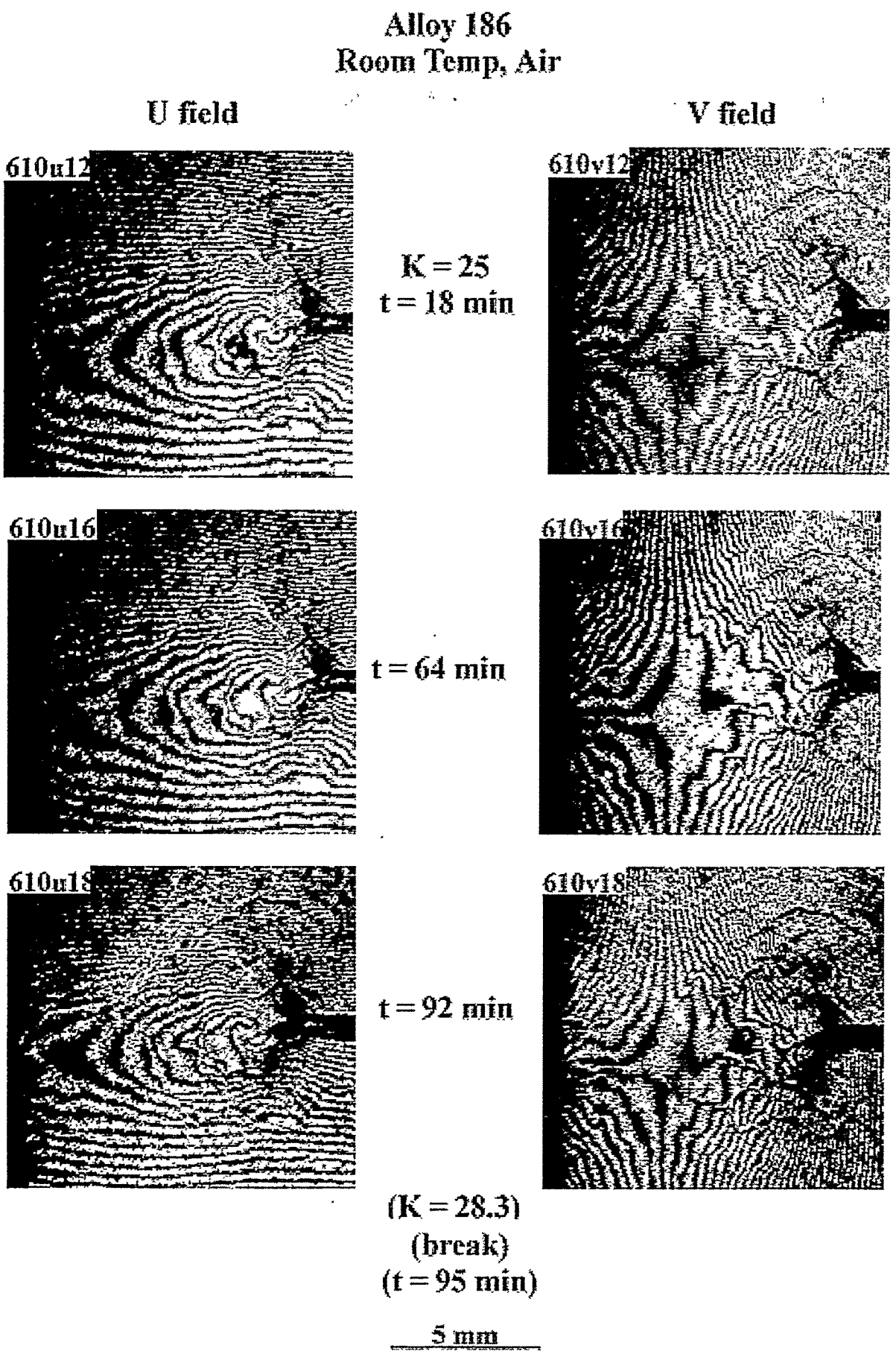

Fig. 4 U and V displacement fields of alloy FA-186 SEN specimen tested in air.

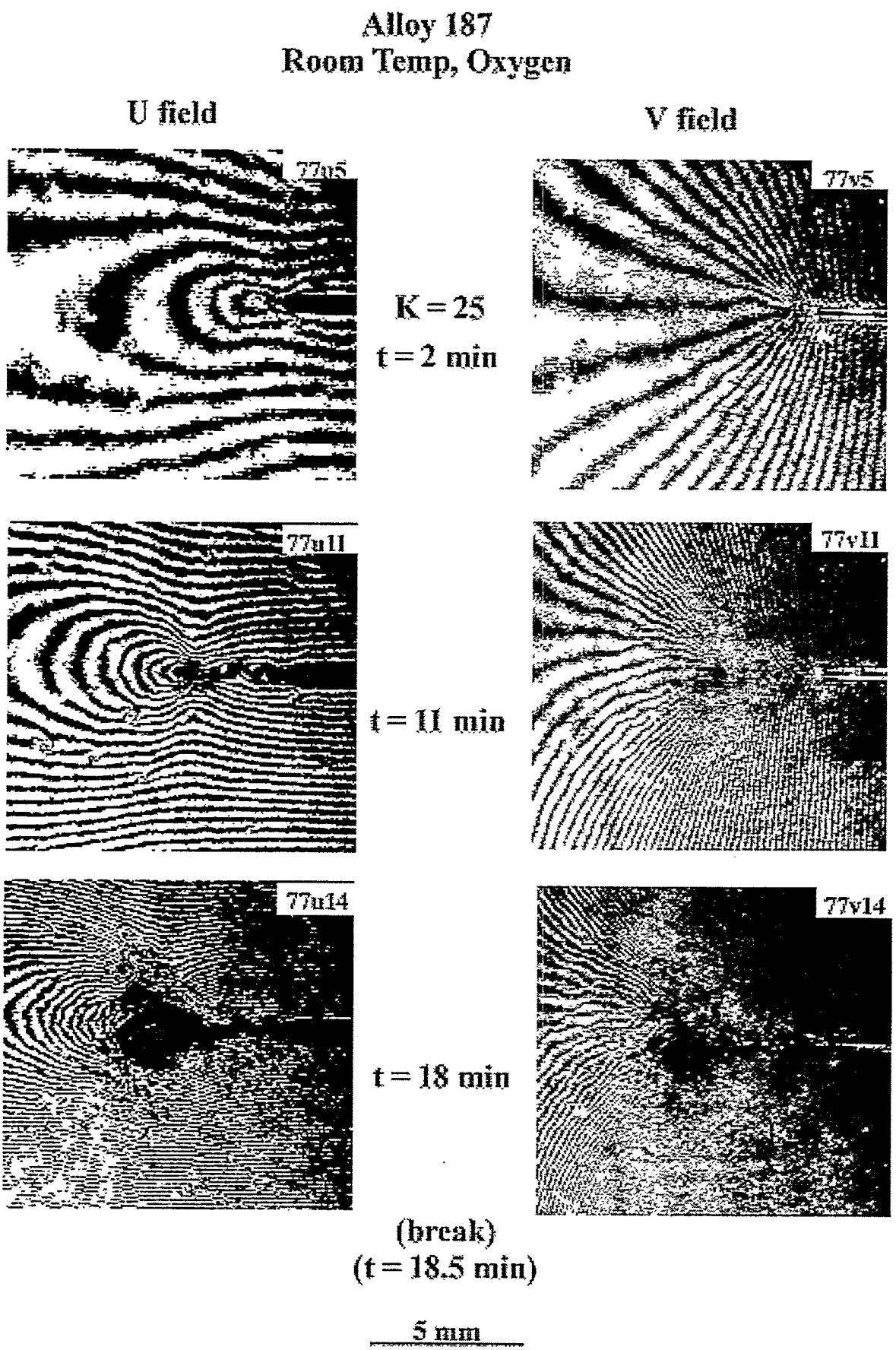

Fig. 5 U and V displacement fields of alloy FA-187 SEN specimen tested in dry oxygen.

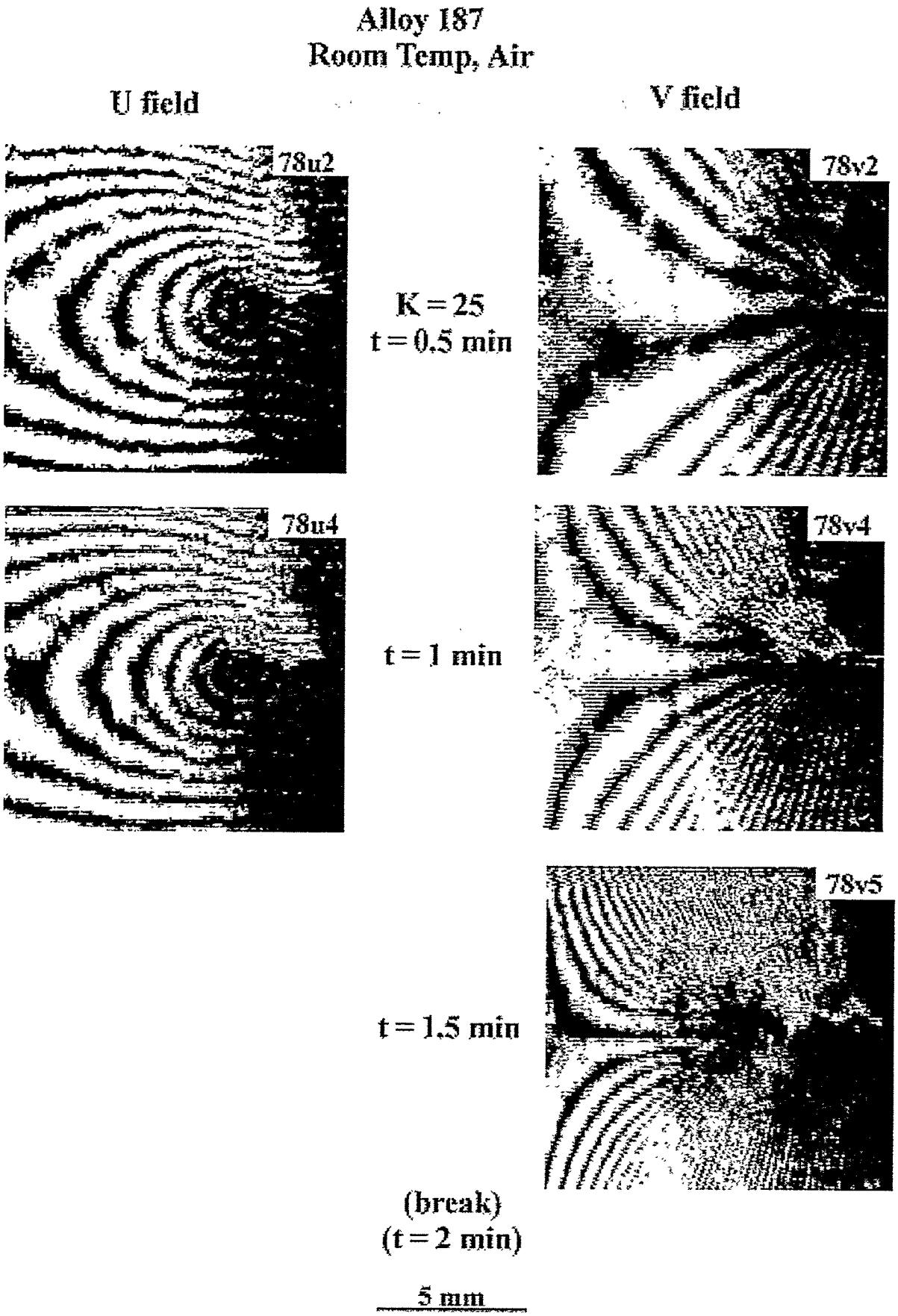

Fig. 6 U and V displacement fields for alloy FA-187 SEN specimen tested in air.

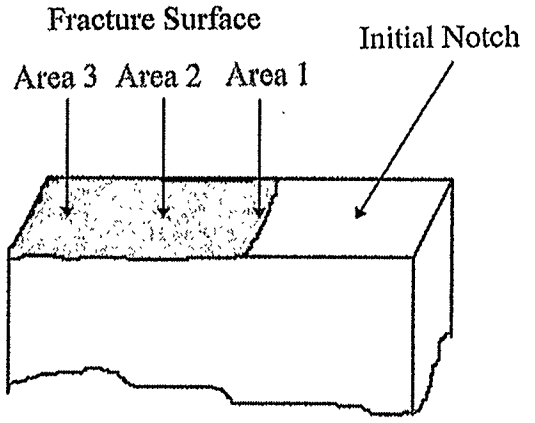

area 3

area 1

FA-186
(Oxygen)

area 3

area 1

FA-186
(Air)

← Crack Growth Direction

Fig. 7 SEM fractographs of alloy FA-186 SEN specimen.

Fig. 8 SEM fractographs of alloy FA-187 SEN specimen.

THE MECHANICAL RELIABILITY OF ALUMINA SCALES AND COATINGS

K. B. Alexander, K. Prüßner and P. F. Tortorelli

Oak Ridge National Laboratory
P. O. Box 2008
Oak Ridge, Tennessee 37831-6376

ABSTRACT

The mechanical integrity of oxide scales ultimately determines their ability to protect materials from corrosion and other environmental effects arising from deleterious reactions with gases and condensable products. The microstructure and mechanical behavior of alumina products thermally grown or deposited on Fe-28 at.% Al intermetallic alloys are being characterized in order to develop the knowledge and means to control the mechanical reliability of alumina scales by microstructural manipulation through design and processing.

Mechanical characterization involved gravimetric data from cyclic oxidation experiments, in-situ observation of oxidized specimens undergoing flexural loading in a scanning electron microscope, and measurements of hardness, elastic modulus and cracking resistance by nanoindentation. Values of cracking thresholds for Al_2O_3 scales were consistent with other measurements for surface and bulk alumina.

The oxidation behavior of Fe_3Al alloys coated with a thin (0.5 - 1 μm) alumina film deposited by plasma synthesis has been studied. During exposure in the oxidizing environment, new oxide was formed between the coating and the substrate. The presence of the deposited amorphous oxide inhibited the subsequent thermal oxidation of the metal. Because the thermally grown alumina forms under the deposit, the adherence of the coating is controlled by the strength of the metal/oxide interface that develops during oxidation.

INTRODUCTION

In many high-temperature fossil energy systems, corrosion and deleterious reactions with gases and condensable products in the operating environment often compromise materials performance. The presence of a stable surface oxide (either as thermally-grown scales or deposited coatings) can effectively protect the materials from these reactions if the oxides are slow-growing, dense and adherent to the substrate. The protection these brittle oxide films provide has long been a critical issue, particularly for applications involving severe high-temperature thermal cycles or very aggressive (for example, sulfidizing) environments. The various factors which control the scale/coating integrity and adherence are not well understood. The present multilaboratory collaborative work is intended to define the relationships between substrate characteristics (composition, microstructure, and mechanical behavior) and the

structure and protective properties of deposited oxide coatings and/or thermally grown scales. Through such studies, the ultimate goal is to assure environmental protection through effective processing and materials selection leading to the development of corrosion-resistant, high-temperature materials for improved energy and environmental control systems.

The Oak Ridge National Laboratory (ORNL) work described in this paper is being conducted in collaboration with work sponsored by the Department of Energy's Office of Fossil Energy at Argonne National Laboratory (ANL) and Lawrence Berkeley National Laboratory (LBNL) as well as in concert with on-going interactions that are part of the Office of Basic Energy Sciences' Center of Excellence for the Synthesis and Processing of Advanced Materials. The Center of Excellence on Mechanically Reliable Surface Oxides and Coatings includes participants from ORNL, ANL, LBNL, Idaho National Engineering Laboratory (INEL) and Lawrence Livermore National Laboratory (LLNL). Each of these laboratories has appropriate expertise in areas of materials characterization, modeling, and coating/deposition techniques relevant to studies of oxide scales and coatings.

The initial work is focusing on several model systems, all of which form stable, slow-growing alumina scales at elevated temperatures. Systems were chosen which were relevant to ongoing technological interests as well as to represent a range of both "soft" and "stiff" substrates in order to explore the role of the substrate on the mechanical reliability of the oxide scale. This paper will discuss work on the initial system chosen: alumina scales on iron-aluminum alloys with and without zirconium.

EXPERIMENTAL PROCEDURES

Three iron aluminide alloys have been studied to date. Their compositions and common designations are listed in Table 1.

Table 1. Compositions of iron-aluminum alloys used in this study.

Alloy Designation	Concentration[a] (at. %)				
	Al	Cr	Zr	Nb	Other
FA186	28	5			
FA129	28	5	-	0.5	0.2 C
FAL	28	5	0.1	-	0.05 B

[a] Balance is Fe.

Ingots of these alloys were prepared by arc melting and casting. These were then rolled to a final thickness of between 0.8 and 1.3 mm. Rectangular specimens (typically 12 x 10 mm) were prepared from these sheets. Details of the magnetically-filtered cathodic-arc plasma-synthesis process used to deposit alumina coatings on FA186 and FAL alloys are described elsewhere.[1]

Gravimetric measurements under thermal cycling conditions were used to establish overall corrosion behavior at 1000°C. These cyclic oxidation experiments were conducted in static air by exposing coupons in individual pre-annealed alumina crucibles to a series of 24-h exposures. Scanning electron microscopy (SEM) was performed on oxidized coupons as well as on polished cross-sections through the scale.

A Nanoindenter™ was used to evaluate the mechanical properties of the oxide scales. Hardness and modulus measurements were obtained using a pyramidal Berkovitch indenter. Cracks were generated within the scale for cracking threshold measurements using a cube-corner indenter.[2] For these experiments, a series of indents at different loads were generated across a polished cross-section of a scale. The cracks were subsequently imaged in an SEM.

Room temperature four-point bend testing of oxidized coupons was performed *in situ* in a scanning electron microscope. The geometry of the bending rig is such that the tensile surface of the specimen is continuously observed during loading. The load is continuously monitored and both still and video images of the tensile surface during loading and unloading can be acquired.

RESULTS AND DISCUSSION

The oxidation rate was significantly reduced for the iron-aluminide alloy containing zirconium (FAL) as shown by the thermal-cycling weight gain data in Fig. 1. Distinctive differences were also observed in the morphology of the oxide scales formed on the two alloys. As described previously,[3] the FAL alloy exhibited flat, uniform oxide surfaces with no evidence of spallation during thermal cycling, whereas a significant amount of spallation was observed after thermal cycling of the FA129 alloy, Fig. 2. Cross-sections through the scale on the FAL alloy showed that the scale was completely adherent but exhibited some porosity, Fig. 3. Zirconium-rich particles were also observed at the metal/oxide interface after oxidation of FAL alloys (Fig. 3).

The beneficial effect of zirconium on the oxidation resistance of Fe_3Al alloys is now well-documented over a temperature range of 900-1300°C. [3-5] However, its role in improving oxidation behavior is not well-defined. The present results show that zirconium-rich particles

form at the oxide-metal interface and there is also some evidence that zirconium ions accumulate in the alumina scale.[6] This is consistent with the dynamic segregation behavior observed for reactive-element additions in many alumina-forming systems.[7] Other work has shown that the presence of Zr in the Fe-28Al-5Cr system suppresses segregation of sulfur to the metal-oxide interface. [8]

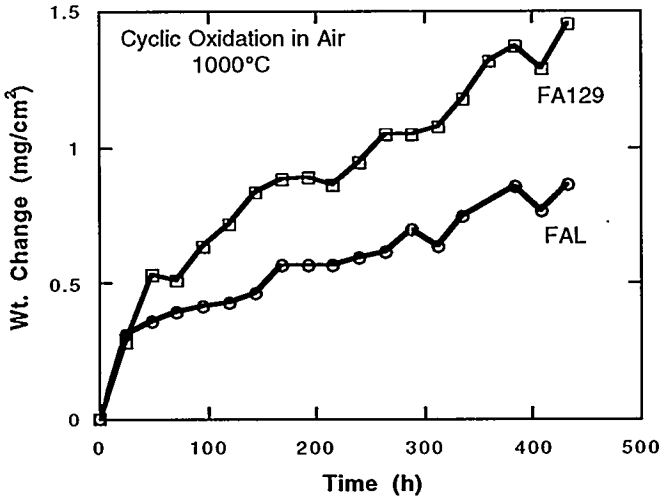

Fig. 1 Total weight gain (specimen + spall) as a function of time for FAL and FA129 cyclically oxidized in air at 1000°C. Each point is a single thermal cycle.

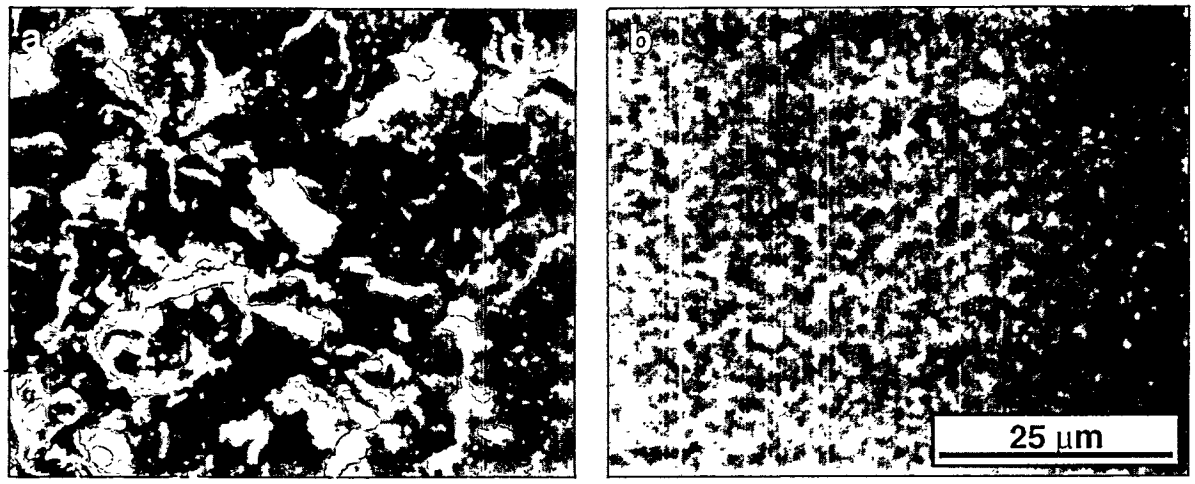

Fig. 2. SEM micrographs of iron-aluminide alloys that were oxidized for 48 h (2 - 24 h cycles) in air at 1000°C. (a) FA129 and (b) FAL. (From Ref. 3)

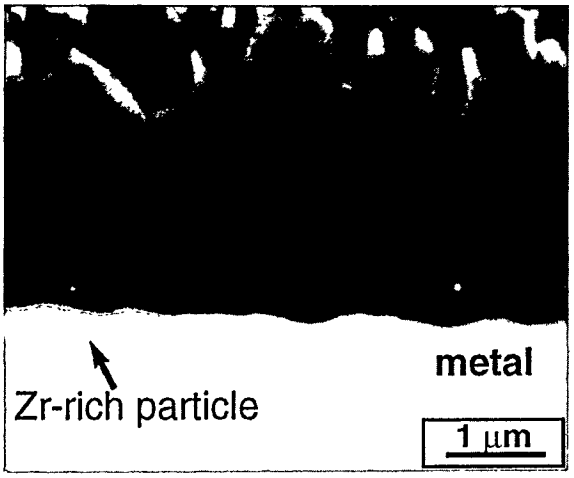

Fig. 3. Back-scattered electron image of oxide scale (2 x 24 h cycles at 1000°) in air) formed on FAL. Porosity within the scale is obvious. Zirconium-rich particles were observed at the metal/oxide interface.

The mechanical reliability of scales depends not only on their intrinsic characteristics such as adherence and defect structure, but also on their response to residual and imposed stresses. For the cracking threshold experiments, performed on an alumina scale grown on FAL, no cracking was detected at 2-μm-wide indents generated with a load of 10mN (1g). Higher loads generated much larger indents and extensive cracking from the corners of the pyramidal indents. The indentation size-indentation load relationship obtained from these experiments is shown in Fig. 4, along with nanoindentation data obtained from single crystal sapphire (indicated as a range).[2]

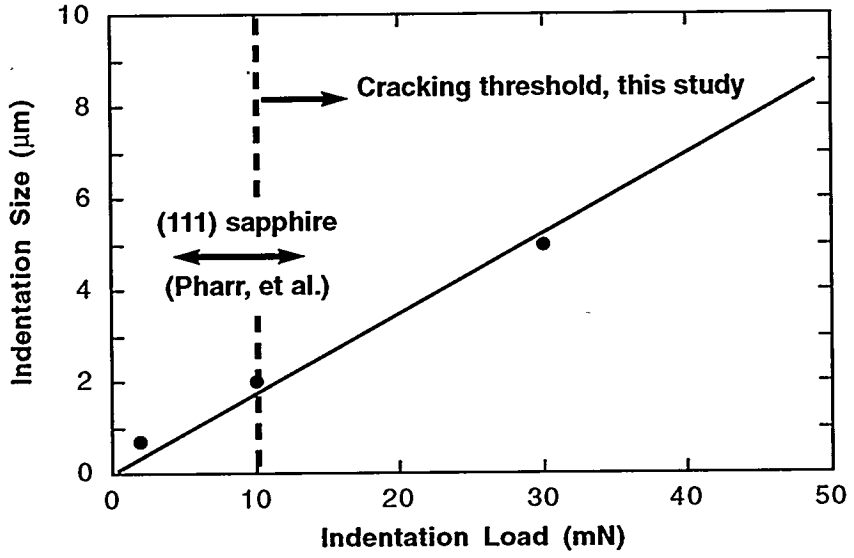

Fig. 4. Indentation size (full width) as a function of indentation load for indents in alumina scale on iron-aluminide. A cube-corner indenter was used for these experiments to attain higher stresses at a given indentation depth and thus induce cracking. Cracks were not observed below the indicated cracking threshold.

Note that the approximate cracking threshold measured for the alumina scale is in agreement with that measured for bulk single crystal α-Al_2O_3. Since cracking was not observed during nanoindentation until the indent was larger than 2 μm, fracture toughness measurements will be problematic since the oxide scale dimensions are typically smaller than the dimensions required to obtain valid indentation crack length measurements. However, the ability to precisely position and create small cracks within the microstructure, especially at or near the metal/oxide interface is encouraging. Such experiments will allow the examination of how crack propagation occurs within the scale and the role of the microstructure on this process.

The four-point-bending experiments also provide information as to how the scale/substrate system responds to imposed stresses. During loading of an FAL coupon with a thin (submicron) oxide scale, sets of parallel, regularly-spaced cracks were observed to spontaneously form on the tensile surface of the specimen after a critical load was reached, Fig. 5. Little growth of the cracks occurred during further loading. Although two sets of nearly orthogonal cracks were observed, the cracking was not perpendicular to the tensile axis. Despite the metal substrate being plastically deformed approximately 30° over approximately 1 cm, the oxide scale remained fully intact with no spallation. Since the scale remained adherent, and cracking was so fine and occurred nearly 45° to the tensile axis, it is suspected that the substrate played a larger role in the deformation process than would be observed for thicker scales. Residual stresses in the oxide may also play a role. The crack spacing and critical load behavior was qualitatively similar to previous bend testing of alumina scales.[9]

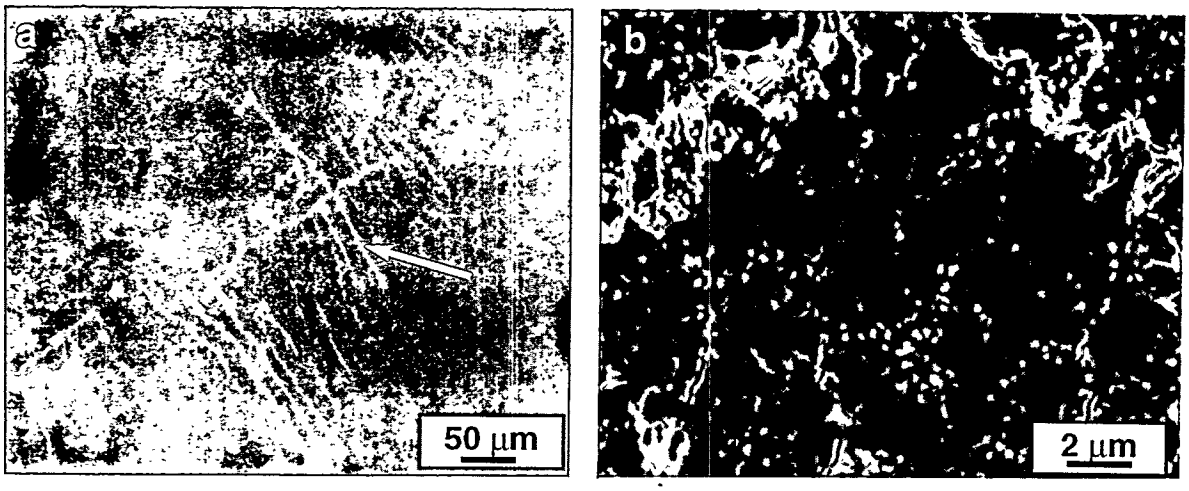

Fig. 5. SEM micrographs of cracking that occurs spontaneously within the scale during four-point-bend loading. The tensile loading direction is horizontal.

The microstructure of the plasma-deposited alumina coatings on FAL was examined in cross-section in the as-deposited condition as well as after exposure for 96 h at 1000°C in air. The surfaces of the deposited films were highly reflective. A comparison between the plasma-deposited alumina film and a thermally-grown scale is shown in Fig. 6. Both the surface and the metal/oxide interface are considerably smoother for the plasma-deposited film. Transmission electron microscopy[10] and X-ray diffraction studies[11] have shown that the as-deposited film is fully amorphous.

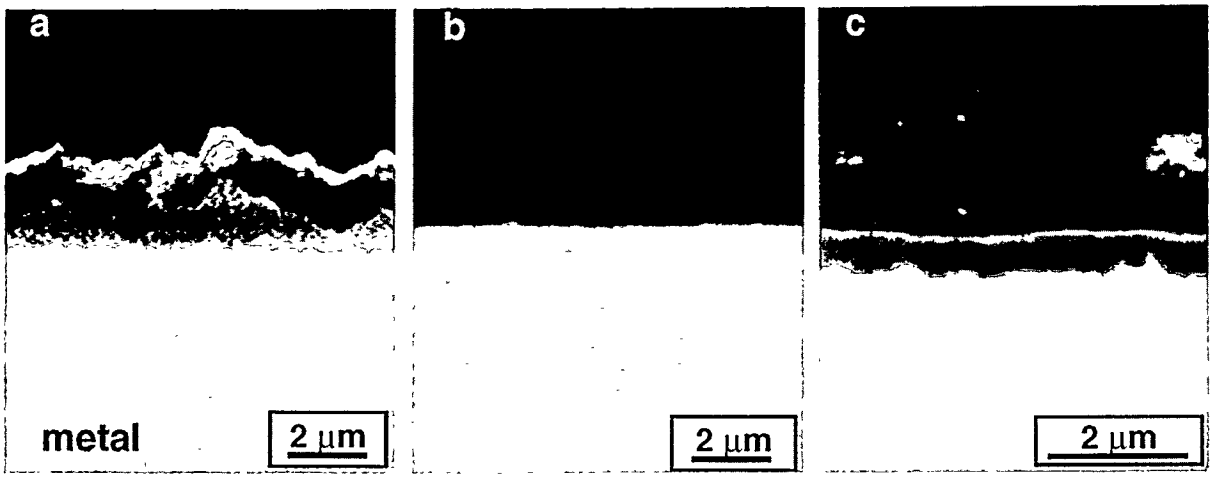

Fig. 6. SEM micrographs of alumina scales on FAL (a) thermally-grown alumina (2 x 24 h cycles at 1000°C), (b) plasma-deposited amorphous alumina, and (c) plasma-deposited film which has subsequently been oxidized for 96 h at 1000°C.

After oxidation (96 h at 1000°C in air), the uncoated FAL specimen exhibited an approximately 2- to 2.5-μm-thick oxide scale. The total alumina thickness after oxidation on a specimen which had been coated with a 0.6-μm-thick plasma-deposited coating prior to oxidation was about 1 μm, as shown in Fig. 7. Zirconium-rich particles were observed at the metal/oxide interface in the case of the uncoated FAL, but not for the coated FAL specimen. A comparison between an as-deposited coating and a coated specimen which had been oxidized is shown in Figs. 6b and 6c. Note that the roughness of the metal/oxide interface has increased, whereas the smoothness of the gas interface has been retained. Auger electron spectroscopy experiments have indicated that the new thermally-grown oxide forms at the metal/oxide interface, beneath the deposited film.[11] Additional experiments on FA186 have confirmed this growth location, since the oxide film (plus thermally-grown oxide) completely spalls from the

metal substrate on cooling consistent with a new thermally-grown oxide/metal interface forming during oxidation and subsequently controlling the adherence in these coated systems after oxidation. [11] These observations are all consistent with the growth of new oxides beneath the deposited film being controlled by the transport of oxygen through the film, rather than by the outward diffusion of aluminum. The presence of the amorphous alumina film obviously diminishes the oxidation rate for the coated FAL alloys, most probably by affecting the transport rate of oxygen and/or by suppressing the formation of the rapidly-growing transition oxides that form initially on bare metal surfaces during oxidation. The absence of zirconium-rich particles at the oxide/metal interface probably reflects diminished oxygen transport through the deposited film.

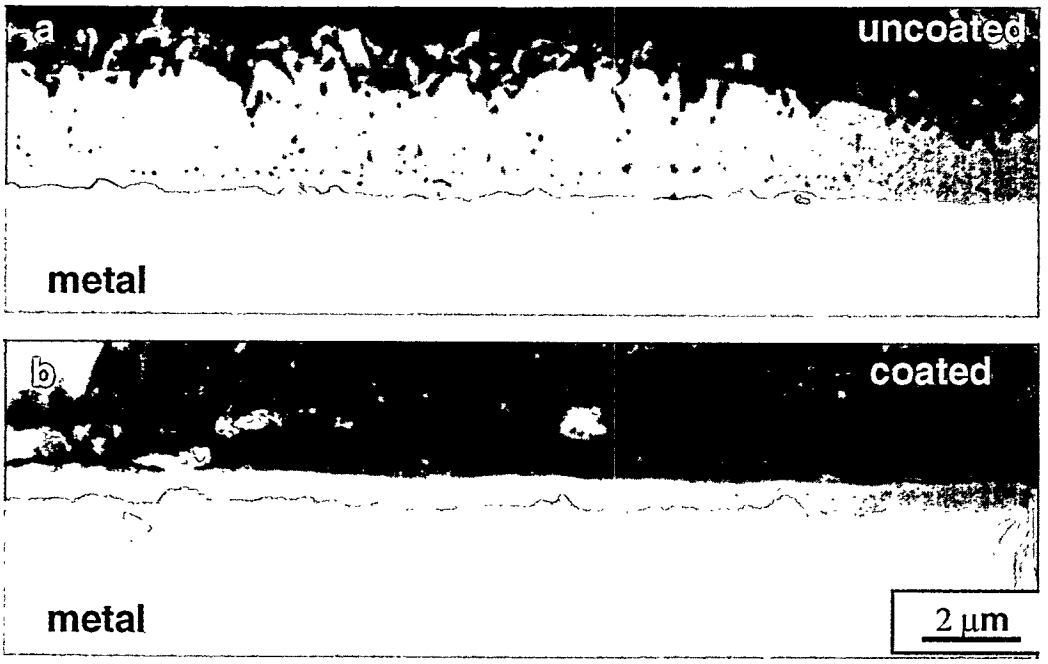

Fig. 7. SEM micrographs showing the effect of an amorphous plasma-deposited coating on the subsequent oxidation behavior of FAL. Cross-sections through oxide scales formed after 96h at 1000°C in air for (a) uncoated FAL and (b) FAL coated with 0.6-μm-thick amorphous alumina prior to oxidation.

SUMMARY AND CONCLUSIONS

The mechanical reliability of scales and coatings can be assessed by traditional means such as gravimetric experiments and observations of adherence (or spallation) during thermal cycling. Other means to establish and study scale adherence such as measurements of the

mechanical properties of scales and their response to stress and/or cracking as a function of processing, composition, and microstructure can also yield important insights into the mechanisms controlling the long-term reliability of protective scales. The adherence of the metal/oxide interface is clearly of the utmost importance as demonstrated by the oxidation experiments on the plasma-deposited coatings. Despite the fact that the oxidation rate was significantly diminished by the presence of the coating, the reliability of the coating was determined by the properties of the thermally-grown oxide/metal interface; which in turn is controlled (in this case) by the substrate composition. This multilaboratory project seeks to further explore and understand the fundamental relationships among properties, structure, and mechanical reliability of surface oxides that provide corrosion protection at high temperatures.

ACKNOWLEDGMENT

The authors thank M. Howell for experimental support. This research was sponsored by the Fossil Energy Advanced Research and Technology Development (AR&TD) Materials Program and the Division of Materials Science, U S. Department of Energy, DE-AC05-96OR22464 with Lockheed Martin Energy Research Corp. Research was performed in part with the SHaRE User Facilities at ORNL.

REFERENCES

1 I. W. Brown and Z. Wang, pp. 239-46 in *Proc. Ninth Annual Conf. Fossil Energy Materials*, N. C. Cole and R. R. Judkins (comp.), CONF-9505204, U. S. Department of Energy, August 1995.

2. D. S. Harding, W. C. Oliver, and G. M. Pharr, Mater. Res. Soc. Symp. Proc. 356 (1995) 663-68.

3. P. F. Tortorelli and K. B. Alexander, pp. 247-56 in *Proc. Ninth Annual Conf. Fossil Energy Materials*, N. C. Cole and R. R. Judkins (comp.), CONF-9505204, U. S. Department of Energy, August 1995.

4.J. H. DeVan, P. F. Tortorelli, and M. J. Bennett, "Environmental Effects on Iron Aluminides," pp. 309 - 20 in *Proc. Eighth Annual Conf. Fossil Energy Materials*, N. C. Cole and R. R. Judkins (comp.), CONF-9405143, U. S. Department of Energy, August 1994.

5. P. F. Tortorelli and J. H. DeVan, pp. 257-70 in Processing, Properties, and Applications of Iron Aluminides, J. H. Schneibel and M. A. Crimp (eds.), The Minerals, Metals, and Materials Society, Warrendale, PA, 1994.

6. J. A. Horton, Oak Ridge National Laboratory, unpublished results.

7. B. A. Pint, Oxid. Met. 45 (1996) 1-37.

8. P. Y. Hou, Lawrence Berkeley National Laboratory, unpublished results.

9. M. M. Nagl, S. R. J. Saunders, and V. Guttmann, Mater. High Temp. 12 (1994) 163-168.

10. K. B. Alexander and K. Prüβner, Oak Ridge National Laboratory, unpublished results.

11. P. Y. Hou, K. B. Alexander, Z. Wang, and I. G. Brown, "The Effect of Plasma Synthesized Alumina Coatings on the Oxidation Behavior of Iron Aluminides", accepted for publication in High Temperature Coatings II, The Minerals, Metals, and Materials Society, Warrendale, PA, 1996.

ELECTRO-SPARK DEPOSITION TECHNOLOGY

Roger N. Johnson

Battelle, Pacific Northwest National Laboratory
P.O. Box 999, K3-59
Richland, Washington 99352

ABSTRACT

Electro-Spark Deposition (ESD) is a micro-welding process that uses short duration, high-current electrical pulses to deposit or alloy a consumable electrode material onto a metallic substrate.

The ESD process was developed to produce coatings for use in severe environments where most other coatings fail. Because of the exceptional damage resistance of these coatings, and the versatility of the process to apply a wide variety of alloys, intermetallics, and cermets to metal surfaces, the ESD process has been designated as one of the enabling technologies for advanced energy systems. Protective coatings will be critical to the life and economy of the advanced fossil energy systems as the higher temperatures and corrosive environments exceed the limits of known structural materials to accommodate the service conditions.

Developments include producing iron aluminide-based coatings with triple the corrosion resistance of the best previous Fe_3Al coatings, coatings with refractory metal diffusion barriers and multi layer coatings for achieving functionally gradient properties between the substrate and the surface. One of the most significant breakthroughs to occur in the last dozen years is the discovery of a process regime that promises an order of magnitude increase in deposition rates and achievable coating thicknesses. Since this regime borders on and exceeds the normal operating limits of existing ESD electronic equipment, development is in progress to produce equipment that can consistently and reliably achieve these conditions for a broad range of materials. Progress so far has resulted in a consistent 500% increase in deposition rates, and greater rates still are anticipated.

Technology transfer activities are a significant portion of the ESD program effort. Notable successes now include the start-up of a new business to commercialize the ESD technology, the incorporation of the process into the operations of a major gas turbine manufacturer, major new applications in gas turbine blade and steam turbine blade protection and repair, and in military, medical, metal-working, and recreational equipment applications.

INTRODUCTION

The objective of this program is to develop an advanced coating process capable of meeting the surface treatment requirements for the next and future generations of advanced fossil energy systems. This includes the development and testing of new materials and coatings with the ability to operate in severe environments beyond current materials limits, and to provide improvements in performance, durability and cost effectiveness for both new and existing power systems. Ultimately new materials performance limits can enable new systems concepts.

A corollary objective is to further advance the Electro-Spark Deposition (ESD) technology and equipment, and to develop broad commercial applications through technology transfer activities.

Just as high performance jet engines would not be possible today without protective metallurgical coatings, so also does the next generation of high efficiency energy systems depend on protective coatings to survive the necessarily higher temperatures and more corrosive environments. The ESD coating process has been designated as one of the enabling technologies for such future systems. One of the reasons for this is that the exceptional structure produced in these metallurgically-bonded coatings makes them virtually immune to damage or spalling under severe service conditions and temperatures that destroy most other coatings. Additional attractions are that the process is portable (allowing coatings or surface treatments to be performed in the field), environmentally benign (creates no noxious wastes, fumes or effluents), and highly cost-effective.

BACKGROUND

The ESD process was developed to provide exceptionally robust coatings for use in nuclear reactor environments when all other commercially available coatings either failed to survive the severe conditions or failed to meet the performance requirements. The Fossil Energy Program leveraged on that success to begin further developing the ESD process,

coatings and applications to meet the demands of advanced fossil energy systems.

Electro-spark deposition is a pulsed-arc micro-welding process that uses short-duration, high-current electrical pulses to weld a consumable electrode material to a metallic substrate. The short duration of the electrical pulse allows an extremely rapid solidification of the deposited material and results in an extremely fine-grained, homogeneous coating that may be amorphous for some materials. The microstructures thus produced are believed to be responsible for the superior corrosion and wear performance usually exhibited by the ESD coatings when compared to similar coatings applied by other processes.

The ESD process is one of the few methods available by which a fused, metallurgically-bonded coating can be applied with such a low total heat input that the bulk substrate material remains at or near ambient temperatures. This eliminates thermal distortions or changes in metallurgical structure of the substrate. Not only is the coating metallurgically-bonded, but it exhibits a functional gradient in composition and properties through the coating thickness. This eliminates the "metallurgical notch" associated with coatings that have an abrupt property change at the coating/substrate interface. The elimination of this notch and the metallurgical bond makes ESD coatings inherently more resistant to damage and spalling than the mechanically-bonded coatings produced by most other low-heat-input processes such as detonation gun, plasma spray, electro-chemical plating, etc. Nearly any electrically-conductive metal, alloy, intermetallic, or cermet can be applied by ESD to metal substrates.

Further background information on the ESD process is provided in Ref. 1 and 2.

DISCUSSION OF PRIOR ACTIVITIES

Chromium Carbide Experiments

ESD coatings usually show lower corrosion rates in most environments than the same material would in either bulk form or as a coating applied by other processes. For example, ESD-applied coatings of chromium carbide-15% Ni exhibit significantly lower corrosion rates in aqueous and liquid metal environments than similar detonation-gun applied coatings.[3] The

superior performance of the former is attributed to the extremely fine-grained, nearly amorphous structure inherent to the ESD coatings compared to the larger-grained, more heterogenous thermal spray coatings.

In tests at Argonne National Laboratory (ANL), this same ESD chromium carbide-15% Ni coating showed (unexpectedly) four times better sulfidation resistance than Type 310 stainless steel at 875 C.[4] Normally, this composition would not be expected to perform that well because of the strong susceptibility of a nickel matrix to sulfidation attack. Again, the near amorphous structure is believed to be a major factor in the corrosion resistance. This observation is in agreement with other Fossil Energy Program work that indicates one mechanism of improving lifetimes of protective oxide films and scales is to maintain as fine a grain structure as possible.[5]

Iron Aluminide Coating Development

One of the most significant advances in ESD coatings for use in sulfidation environments has been the successful development of Fe_3Al as a coating material. Oak Ridge National Laboratory (ORNL) has demonstrated the exceptional corrosion properties of Fe_3Al in bulk form, but alloying to achieve acceptable mechanical properties while maintaining optimum corrosion resistance appears to be a challenge. One alternative is to use the most corrosion-resistant compositions as coatings. ORNL supplied us with various Fe_3Al-based alloys for use in ESD coating development. The iron aluminide compositions proved to be nearly ideal for use in the ESD process. Consistent, defect-free coatings over 100 μm were applied rapidly, uniformly and economically.

Sulfidation corrosion tests on these initial coatings, however, showed that although the corrosion performance was significantly improved compared to the stainless steel substrate, the corrosion resistance was still inferior to that of the aluminide alloy in the plate form. Further investigation showed that weld-dilution effects with the substrate material had reduced the aluminum content at the surface below the threshold 12% Al that appears to be necessary for good sulfidation resistance.[6,7]

Three methods for increasing the aluminum content ultimately were tried. In the first, a simple process of alloying of the surface by ESD using an aluminum electrode was successful in producing aluminum enrichment, but the resulting structure was excessively cracked.[8] The second technique involved a preliminary coating (by ESD) of the substrate with a refractory metal, such as niobium or molybdenum. The higher melting material serves as a barrier to diffusion of the substrate material into the coating during subsequent ESD coating. This resulted in achieving a surface composition undiluted with substrate elements, and doubled the corrosion resistance.[7] The third method became possible when ORNL produced experimental electrode compositions based on FeAl.[9] This material also proved to be well-suited to the ESD process. Excellent quality, crack-free coatings using the higher Al content material were developed and tested.

DISCUSSION OF CURRENT ACTIVITIES

Improved Iron Aluminide Coatings

Corrosion tests completed at ANL showed that the iron aluminide coatings using the FeAl electrode materials were superior in corrosion resistance to all versions of the Fe_3Al coatings and to the reference 304 and 316 stainless steels.[6] The corrosion conditions included simulated coal gasification and simulated coal combustion environments at 650°C for 1000 hours, both with and without the presence of HCl, as shown in Table 1.

Table 1. Chemistries of gas mixtures used for coating evaluation at 650°C[6]

Test Condition	**pO_2(atm)**	**pS(atm)**	**pCl_2(atm)**	**pSO_2(atm)**	**pHCl(atm)**
Gasification	1.5×10^{-23}	5.6×10^{-10}	-	1.3×10^{-11}	-
Gasif. w/HCl	1.2×10^{-23}	5.2×10^{-10}	1.5×10^{-16}	9.1×10^{-12}	2.1×10^{-3}
Combustion	6.7×10^{-3}	1.4×10^{-35}	-	1.2×10^{-3}	-
Comb.w/HCl	4.9×10^{-3}	1.6×10^{-35}	3.6×10^{-4}	9.1×10^{-4}	1.7×10^{-3}

Coated and uncoated specimens were exposed in the above atmospheres for times up to 1000 hr and were periodically retrieved to measure weight changes at intermediate exposures. Figures 1A and B show the weight change data for Types 304 and 316 stainless steels and for Fe_3Al- or FeAl-coated Type 316 stainless steel after exposure at 650 C to simulated gasification environments with or without HCl. The uncoated alloys exhibited general corrosion and significant sulfidation and localized pitting corrosion. The weight gains and scaling rates were much lower for all the aluminide-coated specimens than for the uncoated alloys. The figure shows two curves for Fe_3Al-coated specimens that were fabricated at different times using somewhat different deposition parameters and tested in the same environments but at different times. The data for the two specimens are similar, indicating that the corrosion performance of these coated alloys is reproducible and that substantial improvement in corrosion resistance can be achieved by the surface coating of structural alloys. The best performance was achieved with the specimens having the highest aluminum content in the surface, i.e. those coated with the FeAl.

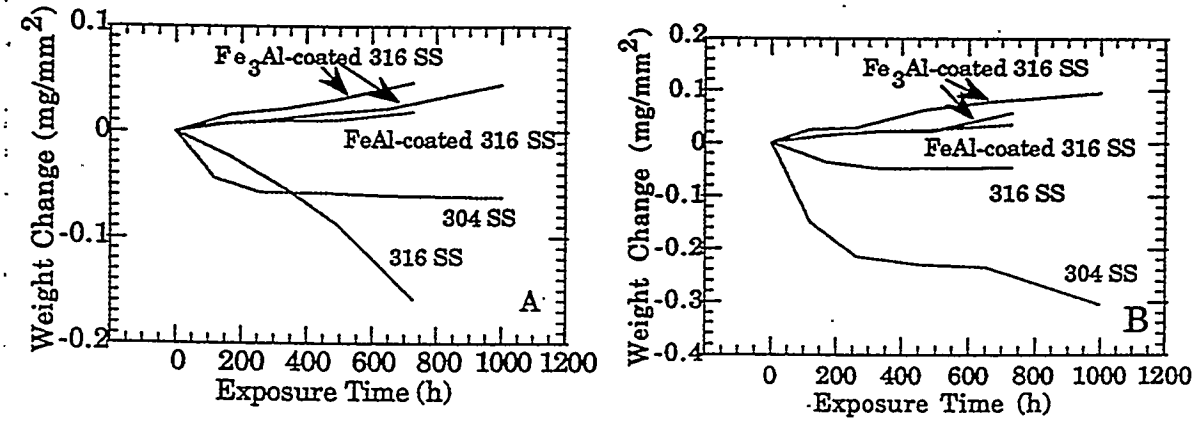

Figure 1. Weight change data for base and aluminide coated alloys tested at 650 C in simulated gasification atmospheres (A) without and (B) with HCl. [6]

Figures 2A and B show weight change data for Types 304 and 316 stainless steels and for Fe_3Al- or FeAl-coated Type 316 stainless steel after exposure at 650 C to simulated combustion environments with or without HCl. In the absence of HCl, the uncoated alloys developed scales of (Fe, Cr) oxide or Fe oxide and tended to crack and spall, as evidenced in

the weight loss in Fig. 2A. The aluminide-coated alloys showed a small weight gain due to the development of a thin, adherent alumina scale. In the presence of HCl, both the uncoated and coated alloys showed increasing weight loss at 650 C. The attack was most notable in the Fe_3Al-coated alloy, indicating that a threshold Al concentration is necessary to protect structural alloys in these environments. The attack was less on the uncoated alloys, but was least on the FeAl-coated alloy.

The success of using FeAl as a coating material now opens the potential of not only improving the corrosion resistance of the structural alloys now used in fossil energy systems, but also of even further improving the performance of the Fe_3Al alloys used in structural applications.

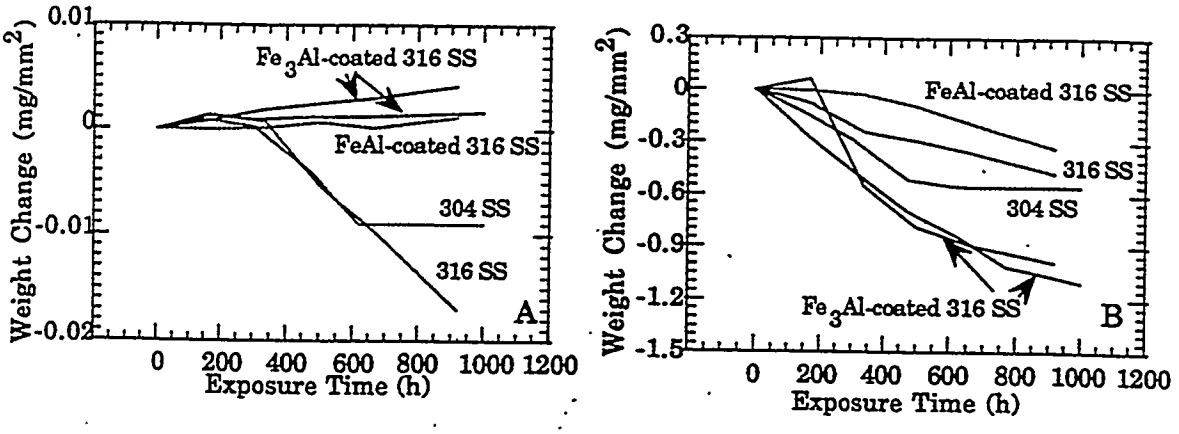

Figure 2. Weight change data for base and aluminide-coated alloys tested at 650 C in simulated combustion atmospheres (A) without and (B) with HCl. [6]

Process and Equipment Development

Exploration of ESD welding parameters at and near the limits of our power supply capabilities has revealed a distinctly different deposition regime for some materials. When this regime is achieved, deposition rates increase by as much as an order of magnitude. The coating thickness limitations usually inherent to most ESD deposits appear to be eliminated. Whereas 100 microns (0.004 in) is normally considered a practical maximum under most circumstances, we have achieved coatings as thick as 1 mm (0.04 in).

This discovery has sparked an effort to develop a next generation power supply that can consistently exploit this regime of deposition parameters without damage to the supply or its reliability. Initial trials showed that in order to achieve the control we believe will provide the desired capabilities, an advanced switching technology most likely will be necessary. However, the particular current and pulse duration requirements that will be needed are beyond the capabilities of all the commercial electronic components so far identified. Until such components become available, we are working to modify the electrical circuits to allow the use of the available state-of-the-art components so far found.

The first prototype of this advanced ESD power supply is now in test. Although the advanced switching technology we had hoped to use still does not meet our requirements, we have succeeded in developing significant increases in deposition rates, typically on the order of 500% increases. This opens further opportunities where the ESD process will be economically attractive for significant commercial applications. Meanwhile, we continue to aim for even greater capabilities that appear to be achievable once adequately robust switching components become available.

Technology Transfer Highlights

A major manufacturer of commercial gas turbine engines is now preparing to incorporate the ESD process into their production line for applying wear-resistant coatings to turbine blades and components. This is the second manufacturer of gas turbine engines to adopt the ESD process, not only because of the cost savings, but also because of the unmatched damage resistance achievable.

ESD coatings on extrusion dies, forging dies and metal working tools are providing life improvements of 300 to 800% in tests at another engine manufacturer. The cost savings reportedly range from $1000 to over $25,000 per die coated.

Test coatings of mixed refractory metal carbides were applied to paper drills for evaluation at a major printing and publishing company. Preliminary indications are that the ESD coated drills are increasing the time between sharpenings by about a factor of six. We

applied the coating in such a way that resharpening can be done without need for recoating. Commercialization of this application appears assured.

REFERENCES

1. R.N. Johnson, "Principals and Applications of Electro-Spark Deposition," *Surface Modification Technologies*, T.S. Sudarshan and D.G. Bhat, eds., The Metallurgical Society, January 1988, p. 189-213.

2. R.N. Johnson, "Electro-Spark Deposited Coatings for High Temperature Wear and Corrosion Applications," *Elevated Temperature Coatings: Science and Technology I*, N. B. Dahotre, J.M. Hampikian, and J.J. Stiglich, eds., The Metallurgical Society, October 1994, p. 265-277.

3. R.N. Johnson, "Coatings for Fast Breeder Reactors," in *Metallurgical Coatings*, Elsevier Sequoia, S.A., New York, 1984, p. 31-47.

4. K. Natesan and R.N. Johnson, "Corrosion Resistance of Chromium Carbide Coatings in Oxygen-Sulfur Environments," *Surface and Coatings Technology*, Vol. 33, 1987, p. 341-351.

5. I.G. Wright and J.A. Colwell, "A Review of the Effects of Micro-Alloying Constituents on the Formation and Breakdown of Protective Oxide Scales on High Temperature Alloys at Temperatures Below 700 C," ORNL/Sub/86-57444/01, September 1989.

6. K. Natesan and R.N. Johnson, "Corrosion Performance of Fe-Cr-Al and Fe Aluminide Alloys in Complex Gas Environments," presented at *2nd Int. Conf. On Heat-Resistant Materials*, Gatlinburg, TN, September 1995 (to be published in the proceedings).

7. K. Natesan and R.N. Johnson, "Development of Coatings with Improved Corrosion Resistance in Sulfur-Containing Environments," *Surface and Coatings Technology*, Vol. 3/44, 1990, p. 821-835.

8. R.N. Johnson, "Electro-Spark Deposited Coatings for Fossil Energy Environments," in *Proceedings of the Seventh Annual Conference on Fossil Energy Materials*, ORNL/FMP-93/1, July 1993, p.289-295.

9. R.N. Johnson, "Electro-Spark Deposited Coatings for Protection of Materials," in *Proceedings of the Ninth Annual Conference on Fossil Energy Materials*, ORNL/FMP-95-1, August 1995, p. 407-413.

INVESTIGATION OF AUSTENITIC ALLOYS FOR ADVANCED HEAT RECOVERY AND HOT GAS CLEANUP SYSTEMS

R. W. Swindeman and W. Ren

Oak Ridge National Laboratory
P.O. Box 2008
Oak Ridge, TN 37831

ABSTRACT

Materials properties were collected for the design and construction of structural components for use in advanced heat recovery and hot gas cleanup systems. Alloys systems included 9Cr-1Mo-V steel, modified 316 stainless steel, modified type 310 stainless steel, modified 20Cr-25Ni-Nb stainless steel, modified alloy 800, and two sulfidation resistant alloys: HR160 and HR120. Experimental work was undertaken to expand the databases for potentially useful alloys. Types of testing included creep, stress-rupture, creep-crack growth, fatigue, and post-exposure short-time tensile tests. Because of the interest in relatively inexpensive alloys for service at 700°C and higher, research emphasis was placed on a modified type 310 stainless steel and a modified 20Cr-25Ni-Nb stainless steel. Both steels were found to have useful strength to 925°C with good weldability and ductility.

INTRODUCTION

The objective of the research is to provide databases and design criteria to assist in the selection of optimum alloys for construction of components needed to contain process streams in advanced heat recovery and hot gas cleanup systems. Typical components include: steam line piping and superheater tubing for low emission boilers (600 to 700°C), heat exchanger tubing for advanced steam and topping cycle systems (650 to 800°C), foil materials for recuperators on advanced turbine systems (700 to 750°C), and tubesheets, plenums, liners, and blowback systems for hot gas cleanup vessels (850 to 1000°C).

STEELS FOR LOW EMISSION BOILERS

Alloys such as vanadium-modified 2 1/4 Cr-1 Mo, 2 1/4Cr-1.5W, 9Cr-1Mo, 9Cr-1.5W and 12Cr-1.5W steels are candidates for the construction of piping, headers, and tubing in the low emission boiler (LEB) project supported by the Pittsburgh Energy Technology Center. However, these classes of steels exhibit a complex metallurgical constitutions that

are not fully understood, and concerns exist about long-term embrittlement due to Laves phase precipitation, degradation of weldments due to cavitation cracking, and susceptibility to creep-fatigue damage. Methods for on-line damage assessment are needed as an assurance against component failures. To assist the LEB project contractors in addressing these issues, damage accumulation mechanisms in 9Cr-1Mo-V steel are being studied. These studies involve the continuation of long-time creep testing on aged 9Cr-1Mo-V steel and the examination of correlation methods to relate mechanical behavior time-temperature-stress history. In collaboration with Wright Patterson Air Force Base, a database was assembled to assess the applicability of new deformation and damage accumulation models. Temperature cycling, relaxation, and compression creep tests were performed to expand the database. Good correlations with the new model were developed. Assistance was provided to standards writing groups to assess the acceptability of accelerated cooling for heavy-section components. Creep testing of air-cooled and water-quenched samples was undertaken, and it was found the water quenching was acceptable in terms of the effect of creep strength. Curves for the two metallurgical conditions are compared in Fig. 1.

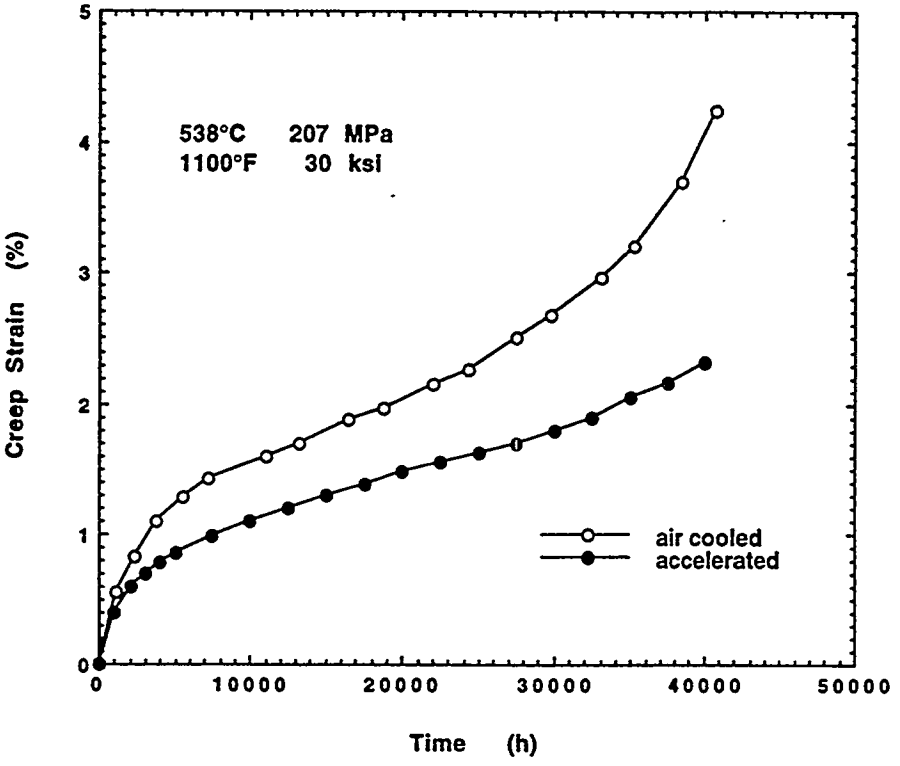

Fig. 1. Comparison of long-time creep curves for 9Cr-1Mo-V steel showing that the creep strength at 538°F is improved by accelerated cooling.

STEELS FOR ADVANCED HEAT RECOVERY SYSTEMS

In the LEB, austenitic stainless steels will be used for tubing in the hotter, more corrosive sections of the superheater and reheater. Candidate steels including niobium-modified 310 stainless steel and titanium-zirconium-modified 20Cr-25Ni-Nb stainless steel. Both steels are limited to approximately 730°C, due in part to a lack of long-time data at higher temperatures. Both steels are candidates for other advanced heat recovery applications, such as low-cost heat exchanger tubing in an advanced topping cycle system or as recuperator foil materials for an advanced turbine system. For both applications, long-time strength, stability, and oxidation resistance are required. Creep testing of modified 25Cr-20Ni-Nb and modified 20Cr-25Ni-Nb stainless steels was started for temperatures in the range of 700 to 815°C, and efforts were begun to examine after-test microstructures. Creep curves for two developmental alloys are compared in Fig. 2 for tests at 760°C and 69 MPa. Both steels have similar rupture lives but the 310TaN stainless steel exhibited a longer period at the minimum creep rate. For components that are strain limited, the 310TaN stainless steel would be preferred.

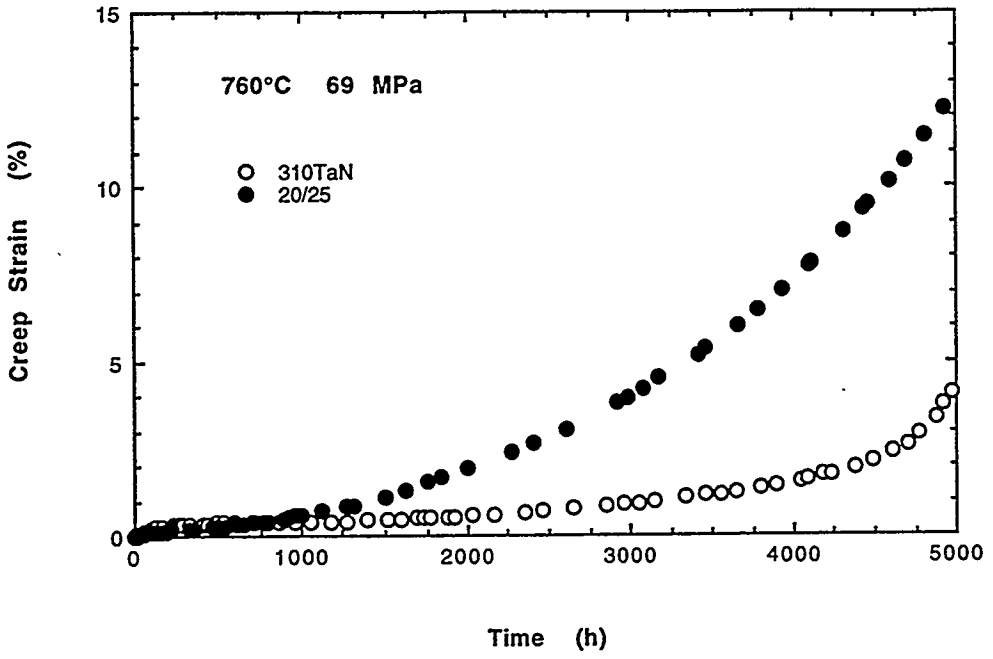

Fig. 2. Comparison of creep curves for 310TaN stainless steel and modified 20Cr-25Ni-Nb stainless steel at 760°C and 70MPa showing the difference in the portion of time spend at low creep rates relative to the rupture life.

ALLOYS FOR HOT-GAS CLEANUP

Components in several advanced fossil energy systems are expected to experience very high temperatures, and the potential for creep damage, fatigue, thermal-fatigue, and creep-fatigue crack growth are significant. For both "code" alloys and developmental alloys, data for design at very high temperatures are often lacking. For these reasons, exploratory research on creep, creep-fatigue, fatigue, and crack growth of several candidate alloys has been in progress.

Earlier work on alloy for hot-gas cleanup involved studies of alloy 333, alloy 556, and alloy 160, which were candidates for use in pressurized fluidized bed (PFBC) hot-gas cleanup systems at temperature above 815°C. More recently, evaluation was begun of the heat of alloy 120 that is the tubesheet material in the hot-gas cleanup vessel installed at the Wilsonville PFBC facility. Testing of alloy 120 includes creep, creep-crack growth, fatigue, and fatigue-crack growth. Fatigue data for alloy 120 are shown in Fig. 3 where they may be compared to other alloys tested at 871°C. Alloy alloys show similar behavior.

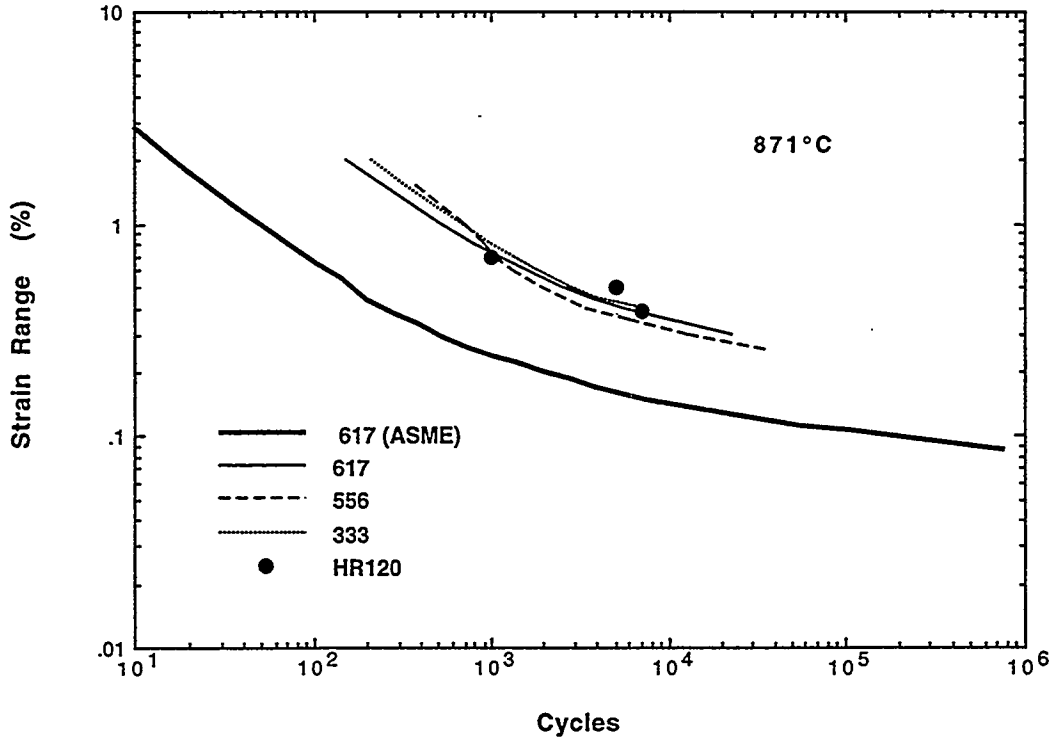

Fig. 3. Comparison of low cycle fatigue data for alloy 120 with other alloys at 871°C.

The modified 25Cr-20 (310TaN) and 20Cr-25Ni-Nb steels are being evaluated for service above 815°C. A comparison of the two steels is shown in Fig. 4 on the basis of the Larson-Miller parameter for rupture. Short-time data indicate that the modified 20Cr-25Ni-Nb steel has slightly better rupture strength properties, but testing of the 310TaN stainless steel has exceeded 30,000 h at 871°C and the performance is excellent relative to standard grades of stainless steels including alloy 800H.

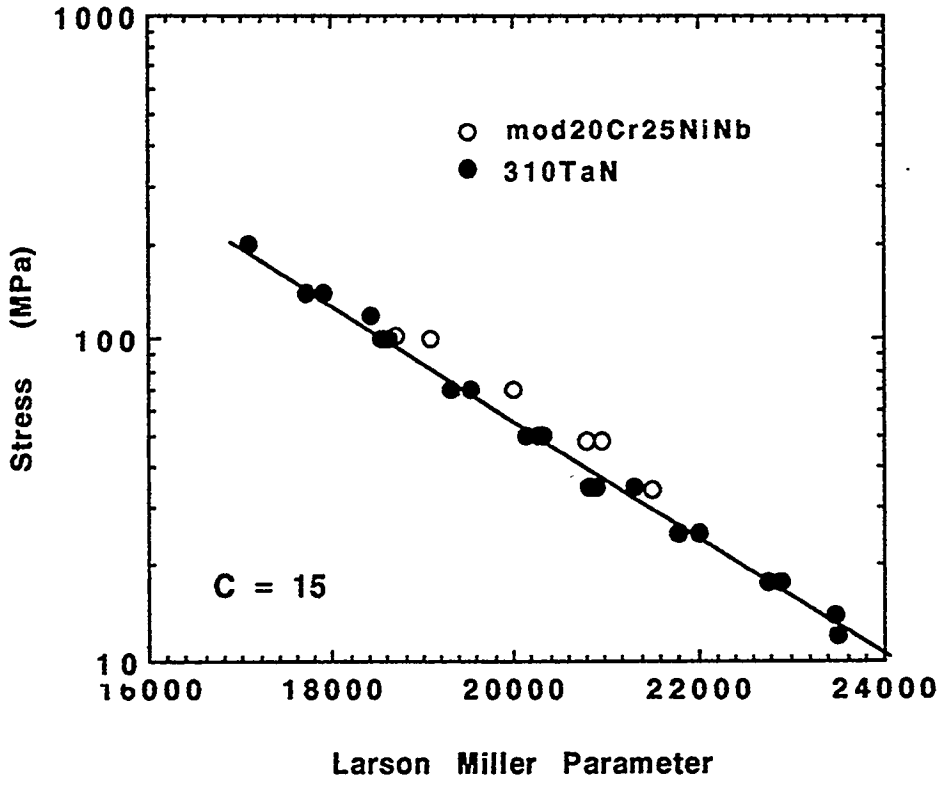

Fig. 4. Comparison of the rupture strength of 310TaN stainless steel with modified 20Cr-25Ni-Nb steel on the basis of the Larson-Miller parameter.

MICROSTRUCTURAL AND WELDABILITY EVALUATION OF 310TaN

C.D. Lundin and C.Y.P. Qiao

Materials Science and Engineering Department
The University of Tennessee
Knoxville, TN 37996

R.W. Swindeman

Metals and Ceramics Division
Oak Ridge National Laboratory
Oak Ridge, TN 37831

ABSTRACT

Excellent weldability and good microstructural stability of 310TaN, in terms of the formation and growth of secondary phases at elevated temperature, was revealed in this investigation. The intergranular stress corrosion resistance of 310TaN is superior to modified 800H and 310HCbN evaluated previously due to the fact that TaC, TaN and Ta(C,N) particles are more stable compared to Nb-rich or Ti-rich carbides, nitrides and carbonitrides presented in the other advanced alloys. Using resistance spot welding technique for which extremely fast cooling is a characteristic, it was found that a very minor amount of grain boundary liquation takes place during welding thermal cycling. The limited grain boundary liquation is of the eutectic type i.e., a low tendency to weld HAZ hot cracking.

INTRODUCTION

310TaN, one of the elite candidates and the newest version of the advanced austenitic alloys, shows excellent mechanical properties at both ambient and elevated temperature. Weldability evaluations have been carried out in terms of weld hot cracking and weld HAZ microstructural stability. This investigation reveals a superior hot cracking resistance for 310TaN compared to other advanced austenitic alloys (including some alloys which are in commercial use).

310TaN exhibits a low weld HAZ softening tendency compared to the other advanced austenitic alloys [1]. Due to the fact that the advanced austenitic alloys exhibit a good general corrosion resistance, the localized corrosion resistance (HAZ), especially for welded fabrication, is of primary importance. The weld HAZ corrosion resistance of 310TaN was examined and it was shown that 310TaN possesses the highest HAZ intergranular corrosion/stress corrosion cracking resistance contrasted to the other advanced austenitic alloys.

It was revealed by metallographic assessment, that the high stability of the Ta-rich carbides and nitrides significantly contributes to the good corrosion resistance and good weldability. The conclusions from this investigation indicate that 310TaN is a very promising alloy for high temperature applications, i.e. for reheater tubing. An evaluation of the long term mechanical property degradation tendency and an optimum filler metal development for 310TaN is a necessity.

MATERIALS AND EXPERIMENTAL PROCEDURES

The 310TaN alloy was prepared at ORNL as plate. The material was cold rolled with the wall thickness reduced from 0.5" to 0.124" and then annealed in an argon atmosphere at 1200°C for one hour. The chemical composition was analyzed at ABB-CE Metallurgical Laboratories and the results are documented in Table 1. Clearly, it is one of the 25Cr-20Ni alloy systems with relatively low S and P (0.001 and 0.003, respectively). With the exception of Ta, the content of all other active carbide/nitride/carbonitride forming alloying elements (Mo, V, Nb, and Ti) is relatively low compared to the advanced austenitic alloys previously studied. Therefore, it was not unanticipated that the Ta-rich carbide/nitride/carbonitride precipitates would be the predominant type in this alloy.

Table 1. Chemical Composition of 310TaN (Heat Number : EJF23-3624).

C	Mn	P	S	Si	Ni	Cr	Mo	V	Nb
0.044	1.56	0.003	0.001	0.25	20.78	24.15	0.01	0.01	<0.01
Ti	Co	Cu	Al	B	N	O	Ta	Ca	Fe
<0.01	0.04	0.06	0.044	0.001	0.19	0.004	1.10	<0.002	Bal.

Varestraint hot cracking tests, Gleeble hot ductility tests, Gleeble simulation techniques and electric resistance spot welding techniques were employed to assess weldability. Only a limited number of tests were performed for each evaluation due to the small amount of material available.

The intergranular corrosion resistance for base metal and weld HAZ was evaluated using two ASTM standard testing methods namely; A262 Practice A and Electrochemical Potentiokinetic Reactivation (EPR). Both testing methods assess the tendency for intergranular corrosion and intergranular stress corrosion cracking.

Aging studies were carried out in order to assess the mechanical and metallurgical behavior for long term service at elevated temperature. Two groups of samples were utilized in

the aging effect study. The first group of samples was extracted from creep tested specimens (creep tests were conducted at ORNL) for which the thermal parameters (time and temperature) were available. The materials in the second group of the aging samples were prepared using the 3 mm 310TaN sheet for thermal aging. The sample surface was carefully cleaned and the material was placed in a quartz tube evacuated and backfilled with argon. A photomacrograph showing the quartz encapsulated samples is exhibited in Figure 1. The aging temperatures selected were: 600°C, 800°C, 1000°C and 1200°C combined with aging times of 1, 10, 100 and 1,000 hours.

Microhardness measurements and metallographic evaluations using OLM, SEM and TEM were conducted in order to provide an explanation for the weldability, aging and corrosion resistance evaluations.

RESULTS AND DISCUSSION

The common weldability issues for structural materials can be classified into two major categories namely, weld metal weldability, which is directly associated with the weld fusion zone chemistry and solidification behavior and the weld HAZ weldability issues (base metal weldability) which are significantly related to the initial base metal composition and conditions. As addressed in the introduction, the base metal weldability of 310TaN is discussed in terms of liquation cracking tendency, weld HAZ softening tendency, microstructural stability, and intergranular corrosion/intergranular stress corrosion cracking resistance. All of the above issues are a function of microstructural changes, such as formation of a partially melted zone, grain growth, and precipitate redistribution (including both precipitate dissolution and re-precipitation during welding thermal history). Recrystallization is not of concern with this alloy because the material was solution heat treated and not cold worked subsequently.

Weldability Evaluation of 310TaN

Varestraint Hot Crack Testing

In the Varestraint hot cracking test, information from all three weld regions (BM HAZ, FZ and WM HAZ) is generated in a single hot cracking test specimen and thus, base metal hot cracking tendency is fully characterized. A summary of the Varestraint hot cracking results is presented in Table 2. According to the Varestraint hot cracking testing criteria [3], the hot cracking tendency in all three zones is low. The cracked HAZ length (CHL) values for two samples tested at 4% augmented strain are 0.70 mm and 0.84 mm which is much smaller than

for 310HCbN (1.25), NF709 (1.36), and modified 800H (1.09). Compared to 310HCbN, the major difference in these alloy systems is that Ta is used in 310TaN while Nb is used in 310HCbN as the MC type carbide forming element. However, a great improvement was found for 310TaN over 310HCbN in terms of hot cracking resistance and weld HAZ softening. It is to be noted that the Fe-Nb and Fe-Ta phase diagrams are similar. However, the eutectic reaction temperature near pure Fe in the Fe-Ta system is 50 C° higher than that in Fe-Nb system and this difference may have contributed to the improved weldability of 310TaN.

Table 2. Summary of Varestraint Hot Cracking Test Results for 310TaN.

Augmented Strain (%)	Weld Metal HAZ		Fusion Zone		Base Metal HAZ		
	MCL (mm)	TCL (mm)	MCL (mm)	TCL (mm)	MCL (mm)	TCL (mm)	CHL (mm)
4	0.16	0.46	0.50	4.71	0.04	0.06	0.77
2	0.10	0.36	0.41	4.62	0.04	0.04	-

* MCL: maximum crack length, TCL: total crack length, cracked HAZ length.

Gleeble Hot Ductility Testing

The hot ductility behavior of 310TaN is indicated in Figure 2 and clearly, a good ductility recovery is noted on-cooling from the ZDT. Therefore, a good correlation between the Varestraint hot cracking and Gleeble hot ductility tests is apparent for 310TaN.

Grain Boundary Liquation Morphology Study

From the work performed in earlier stages [5] of this alloy evaluation program, a HAZ liquation cracking tendency criterion was developed based upon the grain boundary liquation morphologies in a fast cooled resistance spot weld. According to these liquation cracking criteria, if a material exhibits an eutectic reaction related grain boundary liquation it generally possesses a good HAZ liquation cracking resistance. The OLM microstructural morphology in a sample prepared using the resistance spot welding technique is shown in Figure 3. Clearly, the length of liquated grain boundaries is limited in addition to the fact that the grain boundary liquation type is typical of an eutectic reaction related liquation. The HAZ grain boundary liquation study clearly defines why 310TaN possesses excellent HAZ liquation cracking resistance. The grain boundary liquation study also agrees with the weldability predictions from the physical tests.

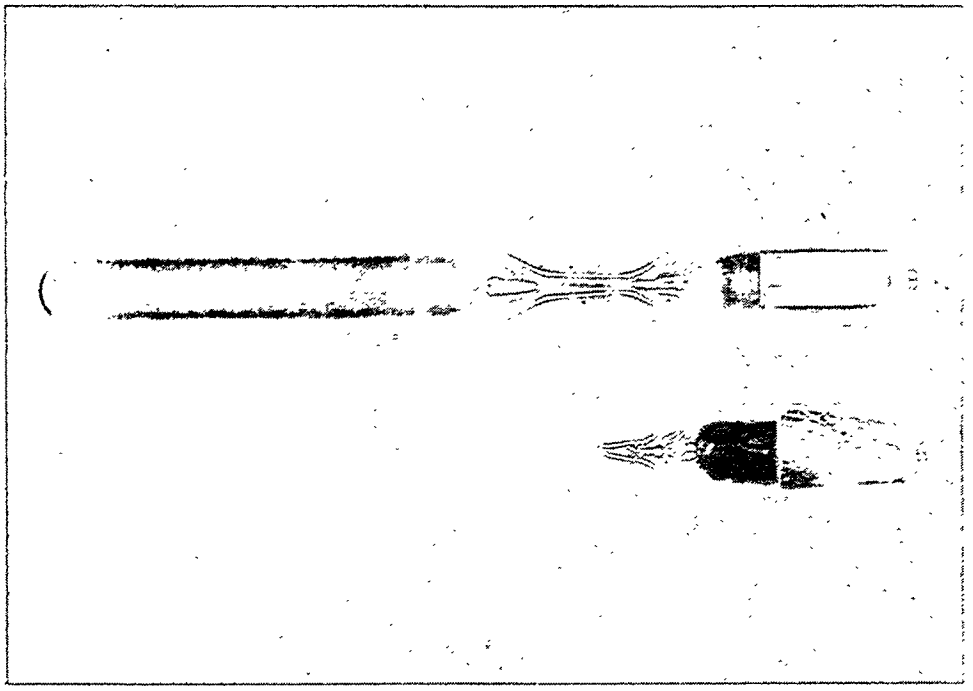

Figure 1. Sealing of sample in quartz tube.

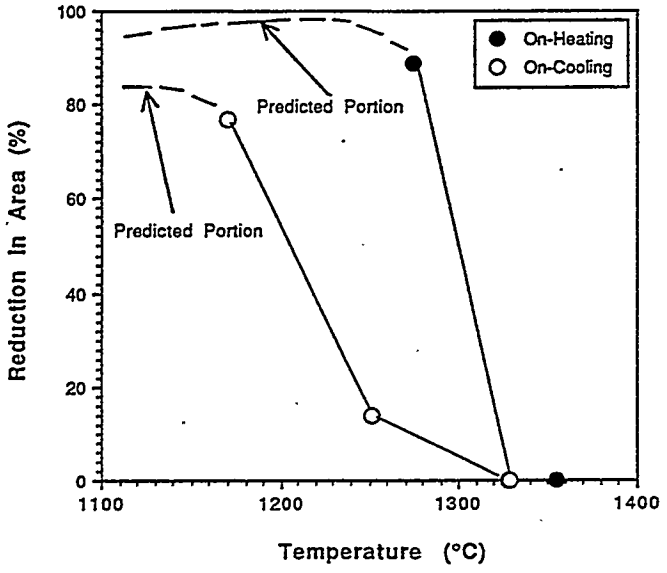

Figure 2. Hot ductility behavior of 310TaN.

Aging Study

Microstructural Characterization

Two groups of samples were used in the aging study, including creep tested samples and virgin aged samples. For the creep tested samples, the material was at elevated temperature for a relatively long time, hence, an extensive amount of secondary phases were formed along the grain boundaries are compared to the average base material. It should be pointed out that strain induced secondary phase formation may have played a rule in these aged samples (depending upon the thermal and mechanical conditions of the creep tests). The OLM microstructural morphologies in the base metal and the creep tested material (982°C, 17.5 MPa for 1794 hours) are indicated in Figures 4a and 4b, respectively.

The virgin aging sample is similar in microstructure to the creep tested samples. Three major secondary phases were found and are categorized in terms of shape and evolution processes and the accuracy of this observation was further confirmed by SEM/EDS. $M_{23}C_6$ type carbides which predominant along the grain boundaries reach a maximum precipitation rate at approximately 950°C for 310TaN. In addition, long term aging at elevated temperature, for instance, at 1000°C for 1000 hours, σ phase starts to form in the 310TaN and thus this may degrade the mechanical properties of 310TaN in the long term. Therefore, a complete solution treatment is important to minimize "harmful" secondary phase evolution.

Hardness Measurements

Hardness measurements were conducted on the creep tested samples as well as annealed base material. The hardness of the creep tested samples is directly related to the type and amount of secondary phases. The harnesses for these aged samples are within a range of 170 to 240HV. If a Larson-Miller parameter is used to assess the thermal effect, the relationship between the hardness and Larson-Miller parameter (°R (C+log t)) is presented in Figure 5. While this is scatter in this limited data set, with an increase in the thermal aging parameter, the hardness of 310TaN increases.

Localized Corrosion Resistance Evaluation

ASTM A262 Practice A

As a screening test, A262 Practice A was conducted on the Gleeble simulated HAZ samples. The basic information from A262 Practice A reveals the tendency and level of the

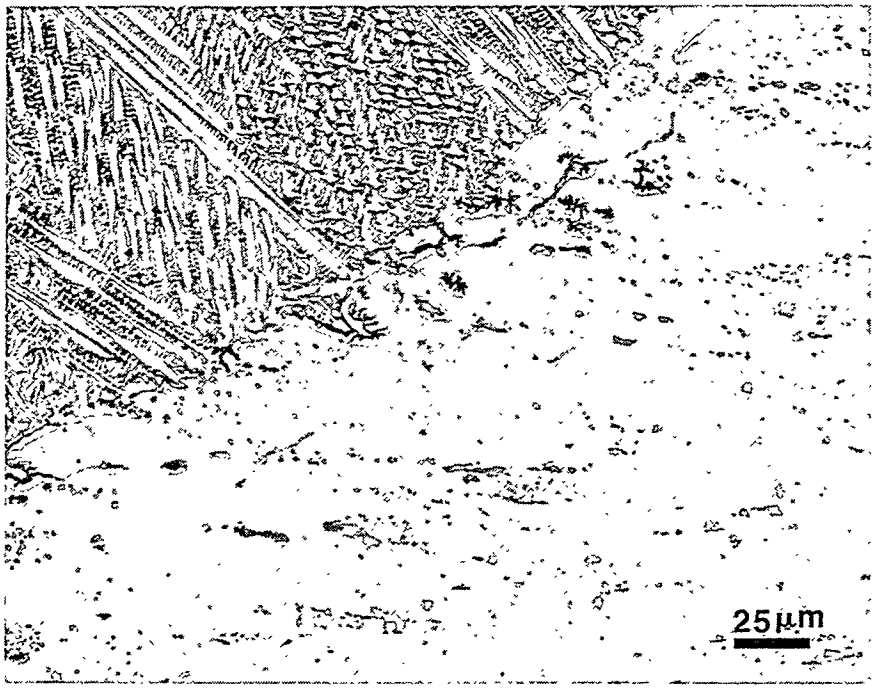

Figure 3. Microstructural morphology in the HAZ of a resistance spot weld in 310TaN.

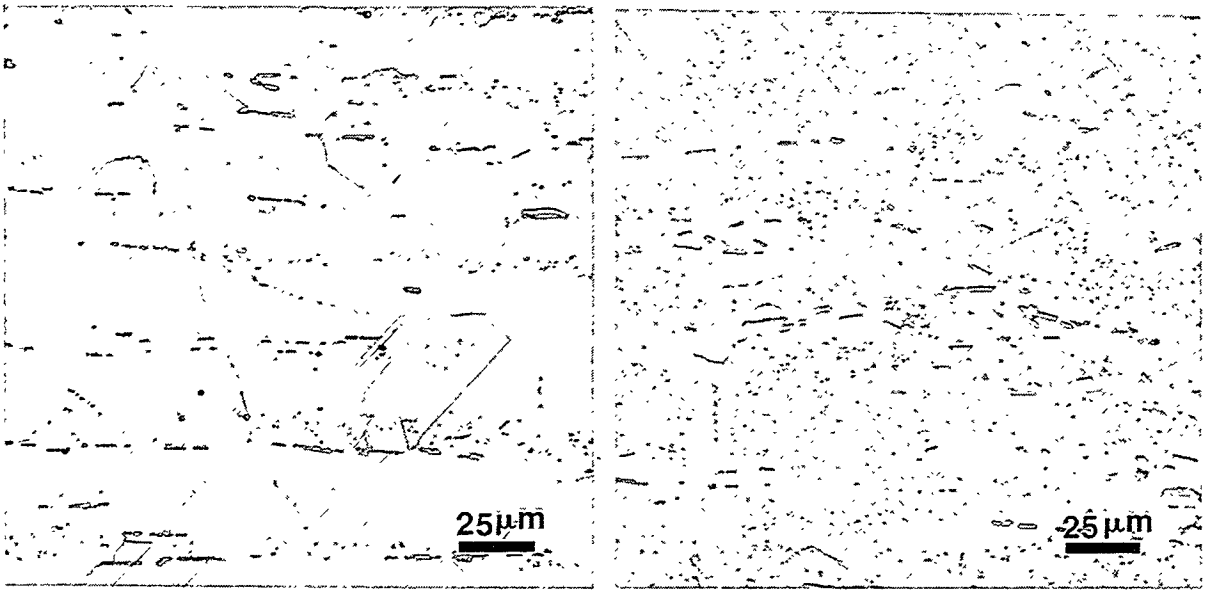

(A) (b)

Figure 4. Microstructural morphologies in (a) the base metal and (b) a creep tested sample (982°C, 17.5 MPa for 1794 hours).

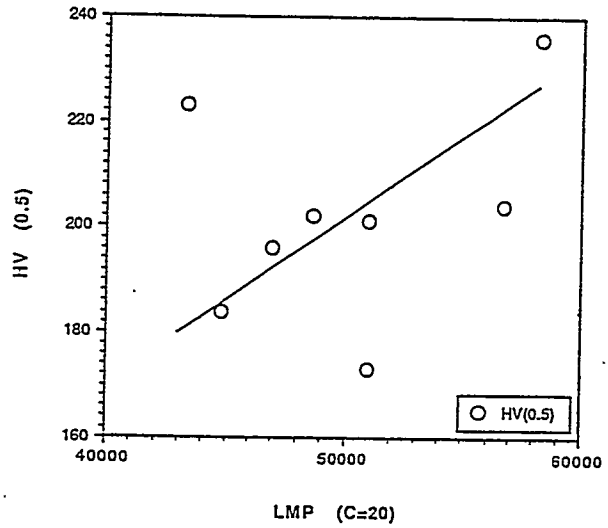

Figure 5. Relationship between the hardness and Larson-Miller parameter (°R (C+log t).

sensitization. A262 Practice A is applicable not only for the weld HAZ but also for base metal. The test results indicate that all samples passed the A262 A screening corrosion test. The sensitization tendencies for the 310TaN base metal and simulated weld HAZ samples are ranked in order: HAZ (PT:900°C), base metal (solution treated at 1200°C for one hour), HAZ (PT:1320°C), HAZ (PT:1200°C), HAZ (PT:1250°C) and HAZ (PT:1100°C). Among them, only the HAZ (PT:900°C) and base metal samples exhibited any ditched grain boundaries although the ditching did not completely surround any entire grain.

ASTM G108 (EPR) Evaluation

The results from electrochemical potentiokinetic reactivation (EPR) evaluations of 310TaN agree with those of ASTM A262 Practice A. All samples used for this evaluation showed only a small weld HAZ sensitization tendency. The EPR test results of the Gleeble simulated samples for 310TaN are presented in Table 3.

Table 3. Summary of EPR Test Results for 310TaN.

Sample	Pa (Test 1) (Coulombs/cm^2)	Pa (Test 2) (Coulombs/cm^2)	Pa (Average) (Coulombs/cm^2)
Base Metal *	0.074	0.044	0.059
HAZ (PT:900°C)	0.038	0.158	0.098
HAZ (PT:1100°C)	0.000	0.035	0.018
HAZ (PT:1200°C)	0.002	0.059	0.031
HAZ (PT:1250°C)	0.006	0.039	0.023
HAZ (PT:1320°C)	0.022	0.069	0.046

* Solution treated at 1200°C for 1 hour.

The Gleeble simulated HAZ (PT:900°C) sample showed the highest sensitization level among this group of samples. This result is understandable since the $M_{23}C_6$ type carbide possesses the highest precipitation rate at about 800 to 850°C for 25Cr-20Ni-Fe alloys. For the case of the weld HAZ, the highest precipitation rate temperature range shifts to higher temperatures due to non-equilibrium heating. Therefore, at a peak temperature of approximately 900°C, the simulated 310TaN weld HAZ possesses the highest tendency to sensitization. It should be noted from this study, that the solution treatment temperature (1200°C) used for the 310TaN is considered slightly low. In order to completely dissolve the secondary phases formed during material fabrication, a higher temperature, such as 1280°C is suggested for the solution treatment. It is expected that the sensitization tendency will be reduced using a higher solution treatment temperature.

CONCLUSIONS

1. The weldability evaluation indicates that the 310TaN alloy exhibits an excellent hot cracking resistance compared to the other advanced austenitic alloys such as 310HCbN, NF709 and modified 800H.
2. Intergranular corrosion resistance of 310TaN is superior to the other advanced austenitic alloys including 310HCbN and modified 800H.
3. Good stability of the TaC, TaN and Ta(C,N) in 310TaN was revealed in the aged and the physically simulated weld HAZ samples and the good thermal stability of these Ta-rich precipitates present in 310TaN is the one of the reasons for the good weldability, intergranular corrosion resistance as well as improved mechanical properties.

ACKNOWLEDGMENTS

This research was financially sponsored by DOE, through the Fossil Energy Materials Program operated at ORNL managed by Martin Marietta Energy Systems, Inc. The great assistance received from DOE/ORNL managers of R.R. Judkins, N.C. Cole, P.T. Carlson during the course of the investigation is deeply appreciated. The authors also would like thank Professor R.A. Buchanan of the Materials Science & Engineering Department of the University of Tennessee for allowing us to use the corrosion laboratory facilities.

REFERENCES

1. Lundin, C.D., and Qiao, C.Y.P., "Comparative Evaluation of the Weldability of Modified 800H and Other Advanced Austenitic Stainless Steels," pp. 341-351, Proceedings of the Seventh Annual Conference on Fossil Energy Materials, May 1993.

2. Lundin, C.D., and Qiao, C.Y.P., "Preliminary Metallographic Examination of Service Exposed SA 213 (Grade HR3C) Hot Reheat Tubing at TVA Gallatin Unit 2," Technique Report, The University of Tennessee, 1995.

3. Lundin, C.D., and Qiao, C.Y.P., "Standard Varestraint Testing Parameters, Procedures and Criteria," Technical Report, The University of Tennessee, 1993.

4. Swindeman, R.W., "The Potential of Modified 310 Stainless Steel for Advanced Fossil Energy Application," ORNL/TM-12057, March 1992.

5. Lundin, C.D., and Qiao, C.Y.P., "Weldability of Modified 800H Alloy," DOE/ORNL Technical Report, ORNL/Sub/88-07685/04, June 1994.

6. Forde, P.T., "Tantalum in Superalloys," pp. 39-40, Advanced Materials & Processes, Vol. 149, No.4, April 1996.

7. Hansen, M., and Anderko, K., Constitution of Binary Alloys, McGraw-Hill Book Company, Inc., New York, 1958.

FIRESIDE CORROSION TESTING OF CANDIDATE SUPERHEATER TUBE ALLOYS, COATINGS, AND CLADDINGS - PHASE II

J. L. Blough
G. J. Stanko

Foster Wheeler Development Corporation
12 Peach Tree Hill Road
Livingston, NJ 07039

ABSTRACT

In Phase I a variety of developmental and commercial tubing alloys and claddings were exposed to laboratory fireside corrosion testing simulating a superheater or reheater in a coal-fired boiler. Phase II (in situ testing) has exposed samples of 347, RA-85H, HR3C, 253MA, Fe_3Al + 5Cr, 310 modified, 800HT, NF 709, 690 clad, and 671 clad for over 10,000 hours to the actual operating conditions of a 250-MW coal-fired boiler. The samples were installed on an air-cooled, retractable corrosion probe, installed in the reheater cavity, and controlled to the operating metal temperatures of an existing and advanced-cycle coal-fired boiler. Samples of each alloy will be exposed for 4000, 12,000, and 16,000 hours of operation.

The results will be presented for the metallurgical examination of the corrosion probe samples after 4000 hours of exposure.

INTRODUCTION

High-temperature fireside metal wastage in conventional coal-fired steam generators can be caused by gas-phase oxidation or liquid-phase coal-ash corrosion. Gas-phase oxidation is usually not a problem if tube and support materials are selected for their oxidation resistance at operating temperatures and for spalling, flaking, or other reactions to their environment. Coal-ash corrosion, on the other hand, usually results in accelerated attack and rapid metal wastage—even of stainless steels. The cause of this type of corrosion is generally accepted as the presence of liquid sulfates on the surface of the metal beneath an overlying ash deposit[1-4].

While substantial progress has been achieved through laboratory testing, actual utility service exposures are evidently necessary to verify any conclusions drawn from laboratory testing. A number of important environmental parameters cannot be fully simulated in the laboratory[5]:

- The actual composition of the deposits formed on the tubes is more complex than the composition of the simulated ash.
- The SO_3, formed by heterogeneous reaction on cooled surfaces, is variable.
- Very large temperature gradients occur within the ash deposits.
- The ash and fuel gas move past tubes at high velocity; the rate varies with design.
- The composition of the corrosive deposits changes with time.
- Metal and flue gas temperatures fluctuate.

- Fly-ash erosion removes the protective oxides, exposing a clean surface to fresh ash.

Foster Wheeler Development Corporation (FWDC) has performed a number of literature reviews and recent updates discussing the variables affecting the corrosion mechanism[6-8]. Additionally, Foster Wheeler is conducting two sizable research projects—one a laboratory and in situ field testing at three utilities of commercially available alloys[5,9-15] and this program (ORNL-FW2), combining laboratory and field testing to more completely cover the controlling variables for a longer duration[10].

In Phase I of this ORNL program, "Fireside Corrosion Testing of Candidate Superheater Tube Alloys, Coatings, and Claddings," 20 commercial and developmental alloys were evaluated[10]. The coupons of the metals were exposed to synthetic coal ash and synthetic flue gases at 650 and 700°C (1202 and 1292°F) for up to 800 hours.

PHASE II CORROSION PROBE TESTING

In this project, the field tests comprise corrosion probe testing, coal characterization, and deposit/corrosion product analysis. The coals have been analyzed to provide fuel characterization, a deposit analysis data bank, and possibly a corrosivity index for predicting corrosivity under various combustion conditions. The equipment and the procedures for this phase have been previously used and perfected at three different utilities for over 3 years of in situ testing at each station.

The utility for test exposures should be burning an aggressive fuel to adequately evaluate the candidate alloys. The coal being burned at Tennessee Valley Authority's (TVA's) Gallatin Station had been previously analyzed, and numerous corrosion indices predicted high corrosivity in addition to the fact that installed T22 and Type 304SS tubing experienced about 7 years of life in the superheaters and reheaters of Units 1 and 2.

Selection of Materials for Corrosion Probes

FWDC laboratory-tested 20 different materials[10]. Because this quantity was impractical from both an economic and a probe-length standpoint, fewer (the ten listed in Table 1) had to be selected for the field tests. These materials provide a range of compositions and cost for both the commercially available and developmental alloys and claddings.

Field Corrosion Probe Design

The corrosion probes were designed to provide realistic exposures of metal samples to both actual boiler environments and also at the higher anticipated metal temperatures of an advanced plant. The probes are independent from the main boiler, removable without a boiler outage, and have a fail-safe design, one that removes

Table 1. Chemical Composition of Candidate Alloys (%)

Alloy	Cr	Ni	Others
Type 347	17-19	9-13	(Nb + Ta) = 10 × C (min.)
85H	18	15	Al = 1, Si = 3.9
NF 709	20	25	Mo = 1.5, Mn = 1.0, Si = 0.6
690 Clad	30	58	
671 Clad	48	52	
Fe_3Al + 5% Cr	5	---	Al = 17
HR3C	25	20	Nb = 0.4
253MA	21	11	Si = 1.7
310 modified	25	20	Ta = 1.5
800HT	21	32	Al + Ti = 1

them from the boiler if there are any malfunctions. With these features, years of testing will not be compromised with a sudden system overheating.

The probes are being exposed for 4000, 12,000, and 16,000 hours. This is being accomplished by utilizing two probe test locations. At one test location, the probe is being exposed for 16,000 hours. At the other test location, the probe will be removed after 4000 hours and a new probe inserted for the remaining 12,000 hours. The design and operation of the retraction system has been discussed in previous years at this conference[16].

The locations in this plant (shown in Figure 1) were chosen because of cavity access and because they best represent the locations for the reheater or superheater outlet on the "Advanced Cycle" unit.

The ideal coal-ash corrosion probe exposure is if only one coal is being burned at the plant. This practice is not common at many utilities; in fact, many are buying coal on the spot market. Gallatin burns a number of eastern high-sulfur coals, mainly Island Creek, Warrior, Dotiri, and Pattiki, which are known to be corrosive and prone to alkali-iron-trisulfate formation. The Borio Index[17] for these coals typically range from 2.0 to 4.1, and the chloride level is 450 to 3000 ppm.

Post-Exposure Analysis

Exposure Results to Date

The 4000-hour probe was removed and shipped to the laboratory for analysis. The 12,000- and 16,000-hour corrosion probes continued to be exposed in the reheater cavity of the TVA Gallatin Station Unit 2.

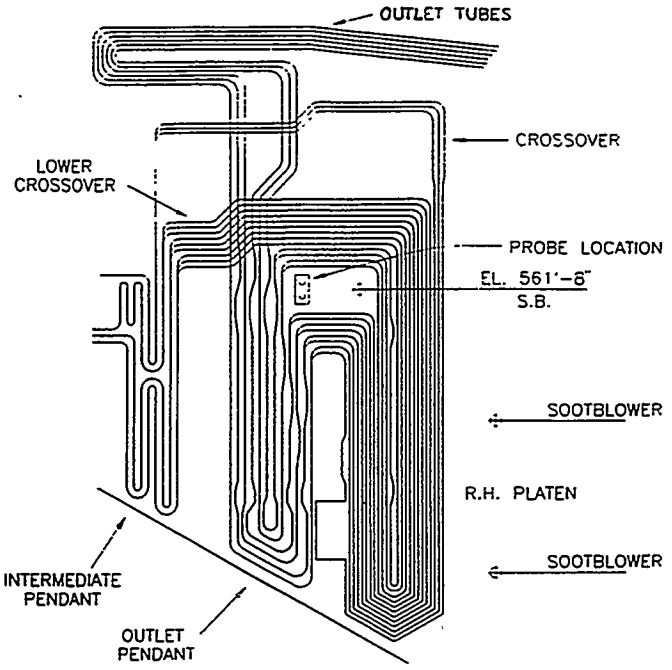

Fig. 1. Side elevation of reheater at TVA Gallatin Unit 2

Macroscopic Examination

The appearance of the transverse cross sections used for the wall thickness measurements is shown in Figure 2. As illustrated, the middle of the sections is approximately the 135-deg location. [Note: Axially oriented grooves, evident at the 180-deg location, are artifacts believed to have been caused by a roller in the guide assembly.] Shallow pitting or surface irregularity is apparent in Samples 1 (85H), 2 (347), and 4 (253MA) in the lower temperature group, and Samples 12 (347) and 14 (253MA) in the high-temperature group. Post-exposure wall-thickness readings were made at the 45-, 135-, and 270-deg locations and the wall loss calculated at the three locations. [Note: Subsequent microscopic examination revealed most of the wall loss in the clad 671 and 690 (Samples 6, 7, 16, and 17) resulted from oxidation of the inside surface which contained a lower alloy concentration from the modified 316 base metal and not corrosion of the outside surface. Oxidation of the inside surface also contributed to the wall loss in Sample 12 (347) and 14 (253MA.] Discounting the high values in Samples 6, 7, 16, and 17 because of oxidation of the I.D. surface, the wall loss values of the specimens in each group were relatively minor. Samples 2 (347) and 4 (253MA) in the lower-temperature group and Samples 12 (347) and 14 (253MA) in the higher-temperature group exhibited higher values than most of the other alloys.

Microscopic Examination

Short sections from the 45-, 135-, and 270-deg locations of the samples were prepared for microscopic and SEM/EDX examination. A summary of the examination follows.

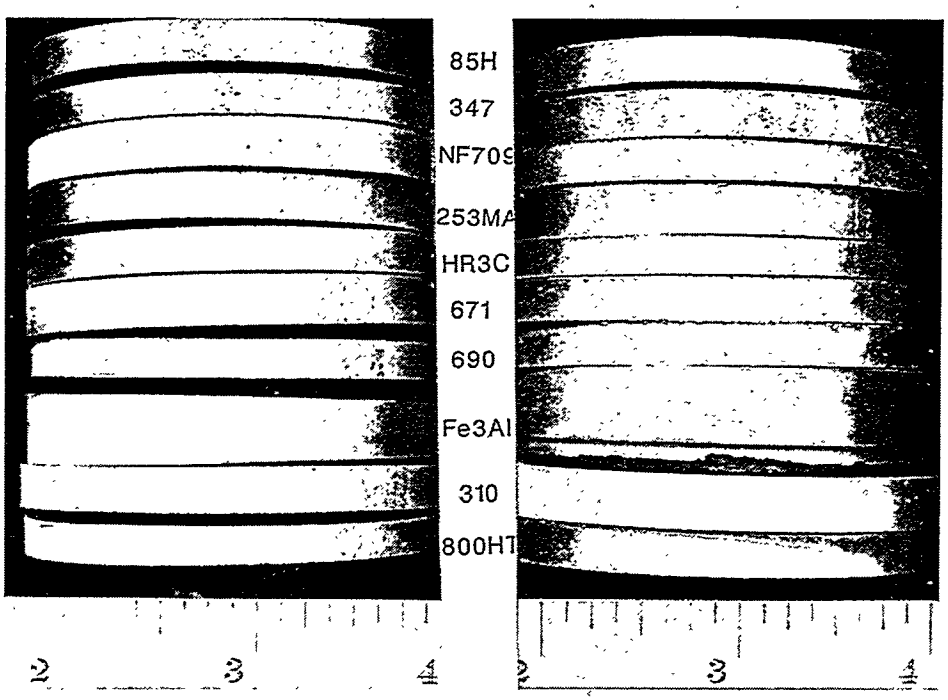

Fig. 2. Cleaned 4000-hour probe.

85H — Both 85H samples exhibited intergranular penetration in the outside surface to a depth of approximately 2.5 mils. Sample 1, which operated at a lower temperature than Sample 11 (1156 vs. 1260°F), displayed more areas of subsurface attack (which is consistent with the observation of the shallow pitting in this sample). Energy dispersive x-ray (EDX) analysis revealed the light gray material in the grain boundaries and pits in Sample 1 was chromium-rich oxide with varying amounts of sulfur. The material at similar locations in Sample 11 was also a chromium-rich oxide but appeared to have less sulfur than the material in Specimen 1. Interestingly, the outside surface at the 270-deg location in Sample 11 also exhibited intergranular penetration to a depth of 2 mils.

Both samples also displayed intergranular penetration in the inside surface. The depth of penetration was 2 mils in Sample 1 and 2.5 mils in Sample 11. This type of penetration is not anticipated to have affected the wall-thickness measurements.

347 — Both 347 samples contained a scale/deposit in the corroded areas. Sulfide penetration to a depth of approximately 0.5 mils below the scale/deposit was also evident in each sample. The outer layer of the scale/deposit was predominantly iron oxide with embedded fly ash particles; the inner layer was a chromium-rich oxide and contained a small amount of sulfur. The sulfides contained iron, manganese, and chromium.

The inside surface of Sample 12 contained a thin oxide with an average thickness of approximately 0.5 mils.

253MA — The 253MA sample in the hotter section (Sample 14) contained a two-layer scale/deposit, with subjacent sulfide penetration to a depth of approximately 1 mil below the scale/deposit. The outer layer was iron oxide, while the inner layer was chromium oxide with notable additions of silicon and sulfur. The sulfides contained iron, manganese, and chromium. The inside surface contained oxide that was approximately 0.8 mils thick.

The outside surface of the sample in the cooler section (Sample 4) also exhibited a two-layer scale/deposit, although it was thinner and present in fewer areas compared to the O.D. scale/deposit on Sample 14. EDX analysis revealed the elemental makeup of the scale layers was similar to those in Sample 14. The degree of internal sulfidation was also lower in Sample 4 and the inside surface was free of scale.

800HT — Both 800HT samples exhibited a two-layer scale/deposit with some minor internal oxidation and sulfidation. The depth of the internal penetration was approximately 1 mil in each sample. The outer scale layer was iron rich and contained embedded fly ash particles. The inner layer was predominantly chromium oxide. The sulfides contained iron, manganese, and chromium.

Modified 310 — The modified 310 sample in both sections contained a thin, chromium-rich scale with embedded fly ash particles. No internal oxidation or sulfidation was noted.

HR3C — For the most part, both HR3C samples exhibited a thin, chromium-rich scale on the outside surface. In a few localized areas on the hotter section (Sample 15), a thicker scale/deposit with subjacent internal oxidation to a depth of approximately 1 mil was noted. The outer layer of the scale/deposit was primarily iron oxide and contained fly ash.

NF 709 — Most areas in both samples contained a thin, chromium-rich scale on the outside surface. One localized area in the hotter section (Sample 13) exhibited internal oxidation and sulfidation to a depth of approximately 1 mil. The sulfides contained iron, manganese, and chromium.

671 — Both samples contained a scale/deposit comprised predominantly of the deposit in the outer layer and a thin, chromium-rich oxide on the metal surface. No internal oxidation or sulfidation was evident. The inside surface (which consisted of Modified 316 stainless steel material) contained a 4-mil-thick oxide in the hotter section (Sample 16) and a 1-mil-thick oxide scale in the cooler section (Sample 6). On the basis of the microscopic examination, the large calculated wall loss from the wall thickness measurements for these samples appears to be the result of the internal scaling. The wall loss from the outside surface is estimated to be less than 1 mil.

690 — Similar to the 671 samples, both 690 samples displayed a thin, chromium-rich oxide on the outside surface. In a few areas in the hotter section internal oxidation was noted to a depth of approximately 1 mil. No sulfidation was detected in either sample. The inside surface (which also consisted of Modified 316 stainless steel material) contained a 2-mil-thick oxide scale in the hotter section (Sample 17) and a 1-mil-thick scale in the cooler section (Sample 7). On the basis of the microscopic examination, the calculated wall loss

from the wall-thickness measurements for these samples also appears to be the result of the internal scaling. The wall loss from the outside surface is estimated to be less than 1 mil.

Fe_3Al — The outside surface of both Fe3Al specimens was essentially free of any scale/deposit. Shallow pits were noted in isolated areas in the hotter section (Sample 18). The material in the pits was predominantly aluminum oxide. Numerous cracks that initiated from the outside surface were evident in both samples. The oxide in the cracks was rich in iron and contained some aluminum.

Wastage Determination

Wastage is considered the sum total of wall loss and metal rendered ineffective because of internal penetration of corrosive species (e.g., oxides, sulfides). Since only the wastage from the outside surface is of concern, wall loss from oxidation of the inside surface must be discounted. On this basis, the wastage of the specimens determined from the macroscopic and microscopic examinations is given in Table 2. In Figure 3 the total wastage is plotted vs. the different alloys in the order of increasing percent of chromium. The 690 and 671 wastage, which is microscopically determined to be less than 1 mil, is plotted as 0.5 mils. With the exception of Fe_3Al, the total wastage decreases with increasing chromium levels. The iron aluminide with only 5 percent chromium has zero wastage. Also, the modified 310 alloy with tantalum has a lower wastage than HR3C with a similar chromium level. Future long-term corrosion probes (12,000- and 16,000-hour) will determine whether this is correct or within the data scatter. Also shown in Figure 3, some of the alloys (85H, NF 709, and HR3C) indicate an increase in wastage rate with increasing temperature while other alloys (347 and 253MA) indicate a peak in the wastage at a lower temperature.

CONCLUSIONS

The air-cooled retractable corrosion probes are working successfully and are providing exposure of each of the ten alloys to two different temperatures. The wastage measurements from the 4000-hour exposure indicate a wastage for 347 of about 2.5 mils. The field measurements indicate the same benefit of chromium in providing corrosion resistance (i.e., the higher the chromium level, the lower the corrosion) as the previous Phase I laboratory testing. The exception to this is the iron aluminide with only 5 percent chromium showed no evidence of measurable corrosion. Also, the 310 modified with tantalum performed better than the same 25-percent chromium HR3C with niobium. The data from the future 12,000- and 16,000-hour probes will further evaluate whether these preliminary findings are true. The mode of attack for most of the samples is oxidation and sulfidation. All of these alloys have considerable coal ash corrosion resistance, and the general metal wastage by a fluxing action is therefore minimal

Future metallographic and corrosion deposit analyses will verify the wastage rates and corrosive attack mechanisms (i.e., coal ash, erosion-assisted oxidation, etc.).

Table 2. Total Wastage of Specimens

Sample	Material	Total Wall Loss (mils)	I.D. Wall Loss From Oxidation (mils)	O.D. Penetration (mils)	Total Wastage (mils)
1	85H	0	0	2.5	2.5
2	347	2.7	0.5	0.5	2.7
3	NF 709	0	0	0.5	0.5
4	253 MA	1.9	0	0.5	2.4
5	HR3C	0.3	0	0	0.3
6	671	4.0	1.0	0	<1.0*
7	690	1.1	1.0	0	<1.0*
8	Fe_3Al	0	0	0	0
9	310†	0	0	0	0
10	800HT	0.5	0	1.0	1.5
11	85H	0.5	0	2.5	3.0
12	347	2.0	0.5	0.5	2.0
13	NF 709	1.6	0	(1.0)§	1.6 (2.6)§
14	253 MA	1.2	0.8	1.0	1.4
15	HR3C	0.8	0	(1.0)§	0.8 (1.8)§
16	671	9.7	4.0	0	<1.0*
17	690	4.9	2.0	(1.0)§	<1.0* (1.0)§
18	Fe_3Al	0	0	0	0
19	310†	0.1	0	0	0.1
20	800HT	0.5	0	1.0	1.5

*Estimated from microscopic examination.
†ORNL modified.
§Localized areas.

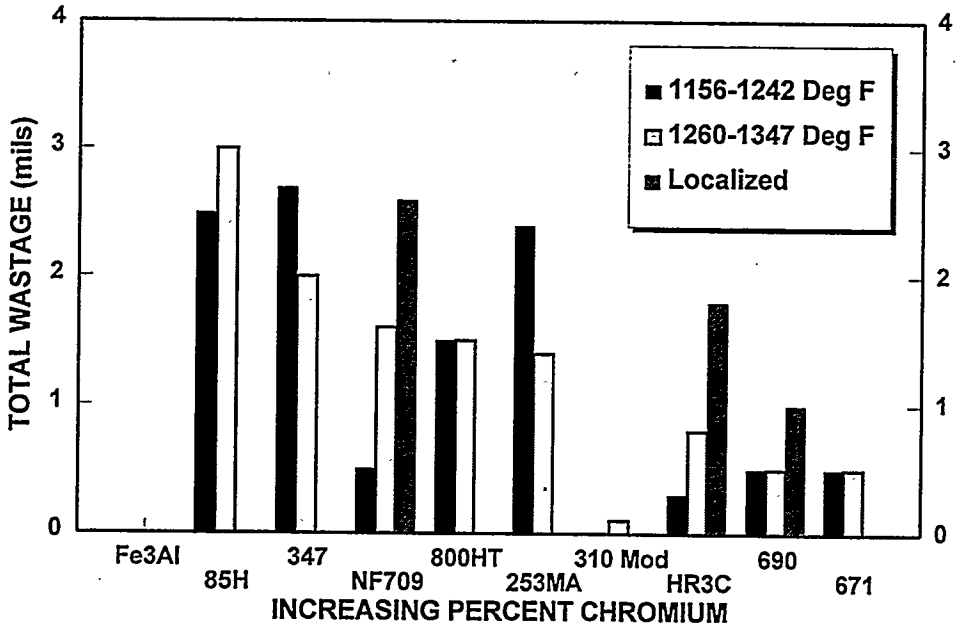

Fig. 3. Total wastage vs. chromium

REFERENCES

1. W. Nelson and C. Cain, Jr., "Corrosion of Superheaters and Reheaters of Pulverized-Coal-Fired Boilers," *Transactions of the ASME, Journal of Engineering for Power,* July 1960, pp. 194-204.

2. W. T. Reid, "Formation of Alkali Iron Trisulphates and Other Compounds Causing Corrosion in Boilers and Gas Turbines," Project Review July 1, 1966-June 30, 1968, prepared by Battelle Memorial Institute, Columbus, OH, June 1968.

3. W. T. Reid, *External Corrosion and Deposits: Boilers and Gas Turbines,* American Elsevier Publishing Company, New York, 1974.

4. G. J. Hills, "Corrosion of Metals by Molten Salts," *Proceedings of the Marchwood Conference: Mechanism of Corrosion by Fuel Impurities,* Johnson and Littler, eds., Butterworths, London, 1963.

5. J. L. Blough, G. J. Stanko, M. Krawchuk, W. Wolowodiuk, and W. Bakker, "In Situ Coal Ash Corrosion Testing for 2 Years at Three Utilities," International EPRI Conference on Improved Technology for Fossil Power Plants New and Retrofit Applications, Washington, DC, March 1-3, 1993.

6. I. M. Rehn, "Fireside Corrosion of Superheater and Reheater Tubes," Palo Alto, CA: Electric Power Research Institute, 1980. CS-1653.

7. I. M. Rehn, "Fireside Corrosion of Superheater Alloys for Advanced Cycle Steam Plants," Palo Alto, CA: Electric Power Research Institute, 1987. EPRI 5195.

8. S. Van Weele and J. L. Blough, "Literature Search Update—Fireside Corrosion Testing of Candidate Superheater Tube Alloys, Coatings, and Claddings," Livingston, NJ: Foster Wheeler Development Corporation, September 1990. FWC/FWDC/TR-90-11.

9. W. Wolowodiuk, S. Kihara, and K. Nakagawa, "Laboratory Coal Ash Corrosion Tests," Palo Alto, CA: Electric Power Research Institute, July 1989. GS-6449.

10. S. Van Weele and J. L. Blough, "Fireside Corrosion Testing of Candidate Superheater, Tube Alloys, Coatings, and Claddings," Livingston, NJ: Foster Wheeler Development Corporation, August 1991. ORNL/SUB/89-SA187/02.

11. S. Kihara, K. Nakagawa, A. Ohtomo, H. Aoki, and S. Ando, "Simulating Test Results for Fireside Corrosion of Superheater & Reheater Tubes Operating at Advanced Steam Conditions in Coal-Fired Boilers, *High Temperature Corrosion in Energy Systems,* TMS/AIME, M. F. Rothman, ed., 1984, pp. 361-376.

12. W. Wolowodiuk, et al., "Coal-Ash Corrosion Investigations," *Proceedings of the First International Conference on Improved Coal-Fired Power Plants.* Palo Alto, CA: Electric Power Research Institute, November 1986.

13. J. L. Blough, M. T. Krawchuk, G. J. Stanko, and W. Wolowodiuk, "Superheater Corrosion Field Test Results," Palo Alto, CA: Electric Power Research Institute, November 1993. TR-103438.

14. J. L. Blough and W. T. Bakker, "Measurement of Superheater Corrosion Caused by Molten Alkali Sulfates," First International Conference on Heat-Resistant Materials, to be presented at the ASM International, Lake Geneva, WI, September 22-26, 1991.

15. T. Hammond, W. Wolowodiuk, J. L. Blough, J. Brooks, "Replacement of Reheater at TVA's Gallatin Station Unit 2," presented at the Third International Conference on Improved Coal-Fired Power Plants (ICPP), San Francisco, April 1991.

16. J. L. Blough, M. T. Krawchuk, and S. F. Van Weele, "Fireside Corrosion Testing of Candidate Superheater Tube Alloys, Coatings, and Claddings — Phase II," Oak Ridge, TN: Oak Ridge National Laboratory, August 1995. CONF-9505204, ORNL/FMP-95/1.

17. R. W. Borio and R. P. Hensel, "Coal-Ash Composition as Related to High-Temperature Fireside Corrosion and Sulfur-Oxides Emission Control," *Transactions of the ASME, Journal of Engineering for Power,* Vol. 94, 1972, pp. 142-148.

PACK CEMENTATION COATINGS FOR ALLOYS

Yi-Rong He Minhui Zheng and Robert A. Rapp

Department of Materials Science and Engineering
The Ohio State University
Columbus, OH 43210-1179

ABSTRACT

The halide-activated pack cementation process was modified to produce a Ge-doped silicide diffusion coating on a Cr-Cr_2Nb alloy in a single processing step. The morphology and composition of the coating depended both on the composition of the pack and on the composition and microstructure of the substrate. Higher Ge content in the pack suppressed the formation of $CrSi_2$ and reduced the growth kinetics of the coating. Ge was not homogeneously distributed in the coatings. In cyclic and isothermal oxidation in air at 700 and 1050°C, the Ge-doped silicide coating protected the Cr-Nb alloys from significant oxidation by the formation of a Ge-doped silica film.

The codeposition and diffusion of aluminum and chromium into low alloy steel have been achieved using elemental Al and Cr powders and a two-step pack cementation process. Sequential process treatments at 925°C and 1150°C yield dense and uniform ferrite coatings, whose compositions are close to either Fe_3Al or else FeAl plus a lower Cr content, when processed under different conditions. The higher content of Al in the coatings was predicted by thermodynamic calculations of equilibrium in the gas phase. The effect of the particle size of the metal powders on the surface composition of the coating has been studied for various combinations of Al and Cr powders.

INTRODUCTION

The search for better high-temperature structural materials has led to the investigation of intermetallic compounds of refractory metal components because of their high melting point, relatively low density, and excellent high-temperature strength[1-5]. Numerous studies have focused on aluminides, silicides, chromides and beryllides. Recently Laves phase intermetallics have received attention.[5,6] Liu and his colleagues[7-13] at Oak Ridge National Laboratory (ORNL) have examined the Cr-Cr_2Nb (Laves phase) alloys. The effects of material processing, heat treatment, and alloying additions on the microstructure and mechanical and oxidation properties of the Cr-Nb (CN) alloys have been evaluated. Hot extrusion at 1480°C was found most effective in repairing casting defects and refining the Cr-Cr_2Nb eutectic structure. Several other beneficial alloying elements have also been identified. However, the oxidation resistance of the CN alloys was not adequate for high temperature application significantly above 1000°C.

To satisfy this need for improved oxidation resistance, silicide coatings on Cr-Cr_2Nb are being investigated in this project. Grabke and Brumm[14] studied the oxidation behavior of $CrSi_2$ in pure oxygen of 0.003-0.66 bar at 900-1200°C; $CrSi_2$ was protective below 1100°C. Douglas et al.[15] concluded that alloys containing Fe, Co,

Ni, Ti and Ta oxidized rapidly at and above 1000°C, but that Cr_3Si was highly oxidation resistant below 1200°C.

The pack cementation method to convert a substrate surface to an oxidation-resistant diffusion coating has the advantages of low cost, good coating adhesion and wide versatility[16]. Previous studies by Mueller, et al.[17,18] showed that a Ge-doped $(MoW)Si_2$ coating on Nb greatly improved its isothermal and cyclic oxidation resistance. As introduced by Fitzer et al.[19] and Schlichting and Neumann[20], the GeO_2 solute formed upon oxidation decreases the viscosity of the protective silica scale. The Ge solute in $MoSi_2$ diffusion coatings, as well as the presence of a residual NaF salt contamination on the coating surface, protects the coating from pesting oxidation at low-temperature exposure[21,22]. Cockeram and Rapp[23] have recently developed an oxidation-resistant Ge-doped Ti-silicide diffusion coating on commercially pure Ti, Ti-22Al-27Nb and Ti-20Al-22Nb alloys in a single step coating process. Therefore, the goal for this work was to develop Ge-doped silicide coatings on the CN alloys.

Prior research at Oak Ridge National Laboratory has led to the development and commercialization of alloys based on the Fe_3Al and FeAl compositions. While these alloys exhibit excellent resistance to oxidation and corrosion, especially sulphidation, at high temperatures, the fabrication of the alloys is difficult and their mechanical properties are problematic. However, these compositions show promise as coatings on strong low alloy steels commonly used in fossil energy applications. The *in situ* CVD process known as pack cementation has the advantages of creating a coating with a true metallurgical bond at the surface of steel components. The pack cementation process involves placing the parts to be coated in a pack of reactive powders, and heating this pack in a retort to an elevated temperature for given time, during which treatment the deposition of a diffusion coating is produced.

A high aluminum content can significantly increase the service life of the components made of FeCrAl-base alloys used at very high temperatures[24]. An aluminum content in excess of 10 wt.% is needed for adequate corrosion resistance in sulfur-containing atmospheres[25]. Geib and Rapp have demonstrated pack cementation Cr-Al coatings for low alloy steel[26], as well as for Fe_3Al[27], using Cr-Al masteralloy powder as the pack constituent.

Economically, it would be beneficial to codeposit Al and Cr in a single batch process to reduce the labor, energy and material costs. The current study is intended to develop a Cr-Al coating on carbon-containing steel surfaces (e.g. T11: C 0.15, Cr 1.0-1.5, Mo 0.44-0.65) by using pure Cr and Al elemental powders instead of a Cr-Al masteralloy, and to avoid the formation of a blocking Cr carbide at the surface. During the sequential process, a substrate is aluminized first at lower temperature and then chromized at higher temperature. During the use of mixed pure Al and Cr powders, alloying of the powders occurs during the processing. Because the finer metal particles have higher surface, the particle sizes have been found to be an important variable in deciding the surface composition.

EXPERIMENTAL PROCEDURES

The CN87 alloy provided by Liu et al.[13] contains 61.5Cr, 8Nb, 1.5Al, 5Mo, 4X2 and 20Fe (at.%) and consists of a Cr-rich phase and the Laves Cr_2Nb phase.

Nominally pure elemental powders of Si (99%) and Ge (99.999%,) were used in the cementation pack. The halide salt activator was NaF (99.7%). Alumina (98%) was used as the inert filler. As the primary means to vary the Ge content in the silicide diffusion coating, variable amounts of Si and Ge were used in various packs. Prepurified Ar gas flowed through the furnace tube to protect the sealed crucible from oxidation. After holding at the coating temperature for a given time, the coupons were retrieved from the pack at room temperature and prepared for metallurgical study.

Cyclic oxidation studies were performed in air in a vertical electric furnace. A K-type thermocouple was used to monitor the temperature. Coupons were placed on an Al_2O_3 mat inside a quartz boat supported by a quartz post, which was moved up and down by a motor. The one hour cycle consisted of 45 minute heating (inside furnace) and 15 minute cooling (outside the furnace).

RESULTS AND DISCUSSION

Figure 1 (a) shows the cross-section of a CN87 alloy coated at 1030°C for 12 hours in a NaF-activated pack containing 20Si-4Ge (wt.%). X-ray diffraction analysis on the coupon surface revealed the existence of Cr_3Si and $Cr(SiAl)_2$. The transitions in phase morphology and distribution are shown in Fig. 1(b). EDS analysis shows that the bright phase in the coating near the surface has the composition 16.3Cr, 13.2Nb, 3.4Mo and 63.8Si with 3.3Ge (at.%), indicating the formation of $(CrNbMo)(SiGe)_2$; the dark phase consists of 28.9Cr, 3.3Mo, 66.8Si plus 0.9Ge, thus a form of $(CrMo)(SiGe)_2$; the gray phase is composed of 26.4Cr, 20.8Fe, 51.3Si plus 1.5Ge, indicating (CrFe)(SiGe).

Figure 2(a) shows the surface morphology of CN-87 alloy coated at 1000°C for 12 hours in a pack containing 16Si-8Ge. The externally deposited nodule phase consisted of 50.2O, 15.0Na, 13.1Al, 12.5Si, 8.5F and 0.6Cl, i. e. an oxide residue from the pack coating process. The bright flakes had the composition of 33.8Na, 27.8F, 21.5O, 10.2Al, 6.3Si and 0.4Cr, i.e. another salt residue. The flat area consisted of 31.7Cr, 4.6Fe, 3.6Al and 60.1Si, indicating the phase of $(CrAlFe)Si_2$. Figure 2(b) shows the cross-section of the coated coupon. A crack traverses the coating but does not enter the substrate; some small voids exist at the substrate/coating interface. Again, the morphology and phase compositions in the coating are closely related to those of the substrate, as expected for dominant inward diffusion of Si and Ge. In the outer part of the coating, the bright phase is $(NbCrMoFe)(SiGe)_2$, the dark phase is $(CrFeMoNb)(SiGe)_2$ and the gray phase is (CrFeMo)(SiGe).

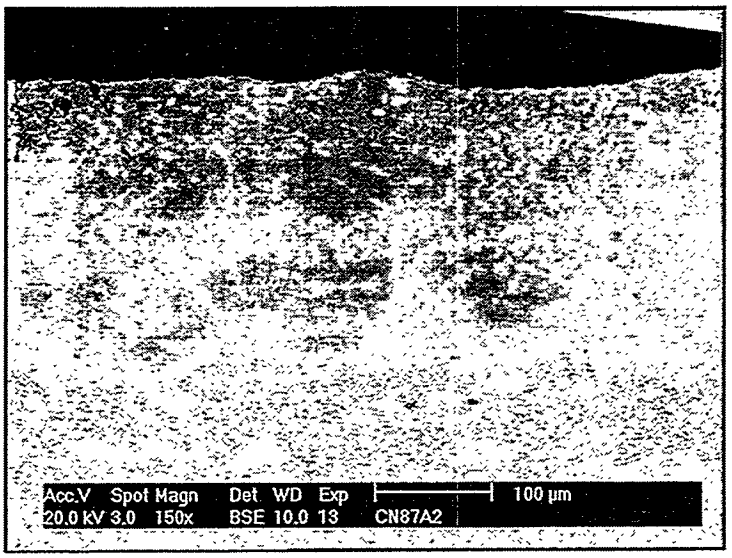

Fig. 1(a) Cross-section of a CN87 alloy coated at 1030°C
for 12 hours in a pack containing 20Si-4Ge

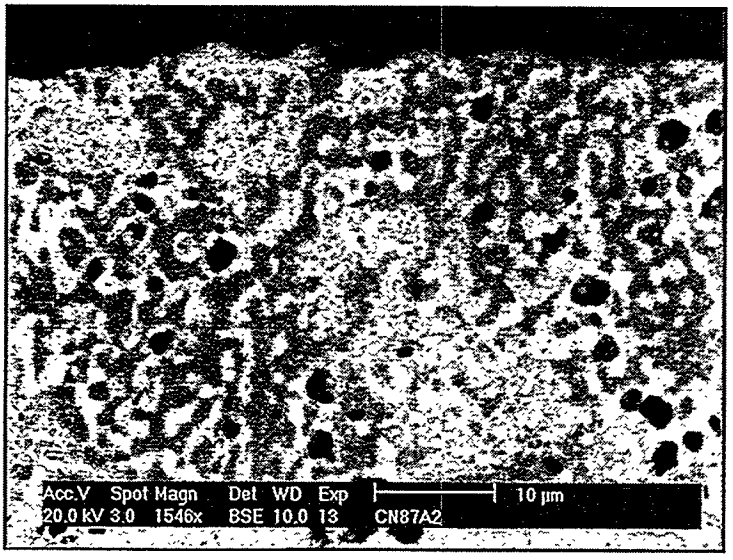

Fig. 1(b) High magnification image of outer part of 1(a)

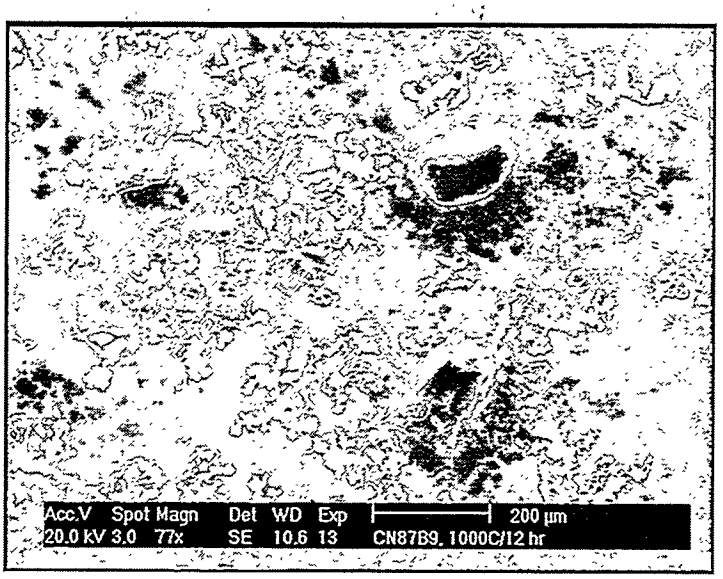

Fig. 2(a) Surface morphology of a CN87 alloy coated at 1000°C for 12 hours in a pack containing 16Si-8Ge

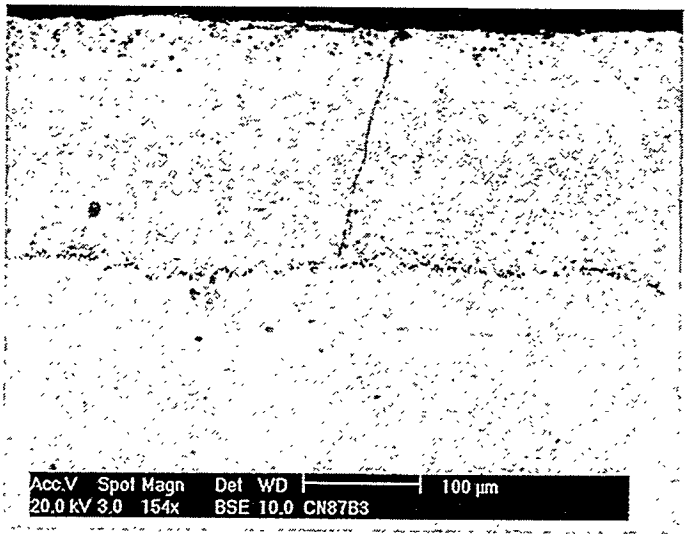

Fig. 2(b) Cross-section of a CN87 alloy coated at 1000°C for 12 hours in a pack containing 16Si-8Ge

Similar characterizations of coatings were made for coatings produced from other packs involving different Si/Ge ratios. Table 1 summarizes the coating characteristics as a function of the Si/Ge ratio in the pack: coating thickness, phases observed, and the highest Ge content and where it was detected.

Table 1 Summary of the characteristics observed in coatings grown from the NaF-activated packs

Si/Ge Ratio	5:1	2:1	1:1	0.5:1	0.2:1
Phases surface to substrate	$M(SiGe)_2$ M(SiGe)	$M(SiGe)_2$ M(SiGe) $M_{11}(SiGe)_8$ $M_5(SiGe)_3$	M(SiGe) $M_{11}(SiGe)_8$ $M_5(SiGe)_3$	M(SiGe) $M_{11}(SiGe)_8$ $M_5(SiGe)_3$	M(SiGe) $M_{11}(SiGe)_8$ $M_5(SiGe)_3$
Coating thickness	233 μm (1030°C)	200 μm (1000°C)	80 μm (1000°C)	83 μm (1000°C)	52 μm (1000°C)
Ge content Region	3.27 (at. %) outer region	2.9 outer region	4.03 inner layer	4.07 inner layer	3.85 inner layer
M represents metal elements					

In general, the morphology and structure of the coatings are complex, which is attributed to the two-phase structure of the substrate and its multiple alloying additions. During the pack cementation treatment, the new phases formed depend on their chemical stability and the diffusion kinetics. Alloying elements partially redistribute among the phases. Therefore, silicides are formed with nominally the same chemical formula but different contents of constituent elements, such as the bright phase of $(NbCrMoFe)(SiGe)_2$ and the dark phase $(CrFeMoNb)(SiGe)_2$ in the same layer.

EDS showed that Ge was not homogeneously distributed in the coatings. As summarized in Table 1, when the pack Si/Ge ratio was less than 1, the highest Ge content was found in the $M(SiGe)_2$ phase in the outermost part of the coatings. When the Si/Ge pack ratio was greater than 1, Ge was concentrated in the $M_{11}(SiGe)_8$ phase of the inner layers. The Ge tended to concentrate in phases with higher Nb content, perhaps because of the larger lattice constants for the high-Nb-content phases. Both $CrSi_2$ and $NbSi_2$ have the same hexagonal structure; the lattice constants of $CrSi_2$ are a = 4.43A, c = 6.37A[28], while for $NbSi_2$ a=4.797A, c=6.592A[29]. Higher Ge content in the pack suppressed the formation of the $CrSi_2$ phase and tended to retard coating growth. A similar effect was observed for the $(MoW)(SiGe)_2$ coating[17] and the Ge-doped Ti-silicide coating[23]. The number of voids formed by vacancy condensation in the inner layer of the coatings also increased with increasing Ge content in the pack, because the coating growth involved more outward diffusion with increasing Ge content in the pack. Cracks were also observed in these coatings. Oxidation attack occurs preferentially

along these pre-existing cracks, but they are sealed by a protective glass formation which prevents penetration to the substrate[17,18].

Two coated CN coupons were subjected to cyclic oxidation in air at 700°C after coating in a pack containing 16Si-8Ge. The residual salt present on the as-coated surface is known to be beneficial in the elimination of pesting for $MoSi_2$[21,22]. To study the effect of the residual salt on the cyclic oxidation behavior, the surfaces of one coated coupon were slightly abraded preliminarily. Figure 3 shows the cyclic oxidation kinetics after 912 cycles at 700°C. Neither coupon exhibited spalling during cyclic oxidation and the weight gains were low: 0.43mg/cm^2 and 0.32 mg/cm^2 for the unabraded and abraded coupon, respectively. Oxidation propagated along cracks in the coating but stopped at the coating /substrate interface.

Two coupons coated in a pack of 16Si-8Ge were oxidized cyclically at 1050°C in air. After 325 one-hour cycles, the weight gains were 4.9 and 4.6 mg/cm^2. For comparison, a CN87 coupon was coated in a pack of 20Si-4Ge, and then tested cyclically for the same conditions. The weight gain was 3.98 mg/cm^2 after 287 cycles. Figure 4 presents the kinetics of these cyclic oxidation tests. X-ray diffraction analysis on the surfaces of the oxidized coupons indicated the existence of Cr_2O_3 (JCPDS 38-1479) and amorphous SiO_2 (JCPDS 29-85). Internal oxidation of Al was also observed in the substrate of the cyclically oxidized coupons.

For the T11 steel samples used in this study of Al/Cr coating, the phase transformation from ferrite (bcc) to austenite (fcc) occurs at 888°C. At a temperature lower than about 920°C, the steel substrate loses weight by $FeCl_2$ evaporation and is not coated well because the vapor pressure of aluminum halide in the pack is not sufficiently high. But for the first treatment step at 920°C or higher, Al diffuses into the surface, serves as a ferrite stabilizer, and pushes carbon into the T11 substrate, as shown in Fig. 5. After the low-carbon ferrite case is formed, Cr can be deposited in the second sequential treatment step at higher temperature, without forming a blocking carbide layer on the surface. The second process step at 1150°C results in a thicker coating as aluminum and chromium diffuse into the substrate. The coatings are aluminum-rich, because of the higher vapor pressure of the Al halide compared to Cr halide. Decarburization was not observed for the substrates with good Al-Cr coatings.

Both the Al and Cr concentrations gradually decrease from the surface to the boundary between the coating layer and the substrate as shown by the EDS results in Fig. 6. Twelve T11 coupons coated in this way were sent to ABB Research Lab. for corrosion testing. After 500 h exposure to simulated boiler gases at 500°C, the coatings were essentially not attacked. Forty more test samples and an steel tube segment have also been coated and are being subjected to extended corrosion testing at ABB.

The reactions of the halide activator(s) with the mixed Cr and Al pure powders in the pack result in volatile metal halides which diffuse and deposit metals on the substrates in the pack. In addition, the volatile species effect an alloying of the Al and Cr pack powders themselves. Kinetically, the transfer of the metal halides is affected by the particle size of pure Al and Cr powders. Consequently, the coating composition was found to vary with the particle sizes of the metal powders in the pack.

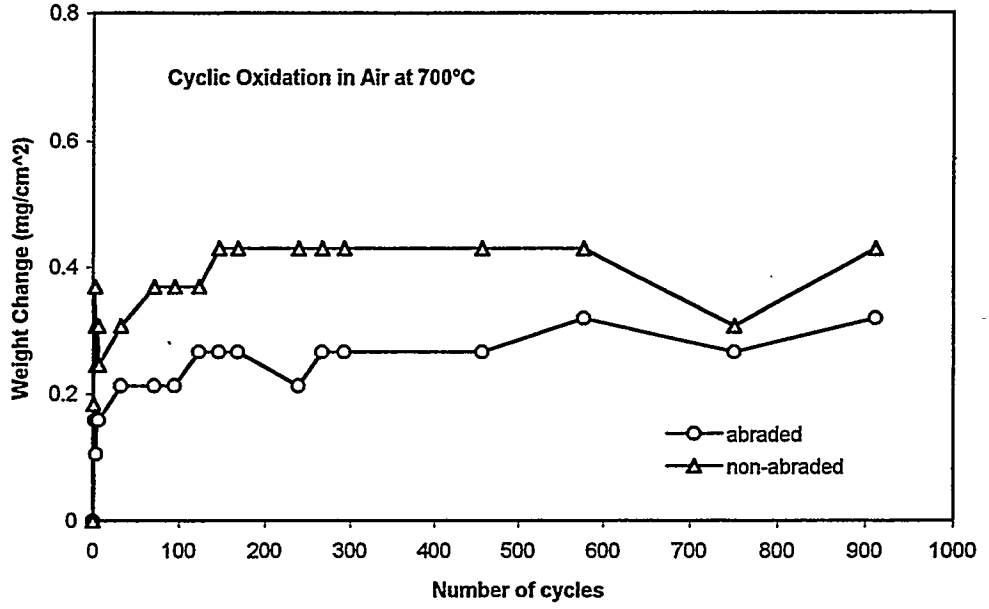

Fig. 3 The cyclic oxidation kinetics at 700°C for duplicate coupons of CN87 coated for 12 hours at 1000°C in a NaF-activated pack with 16Si-8Ge.

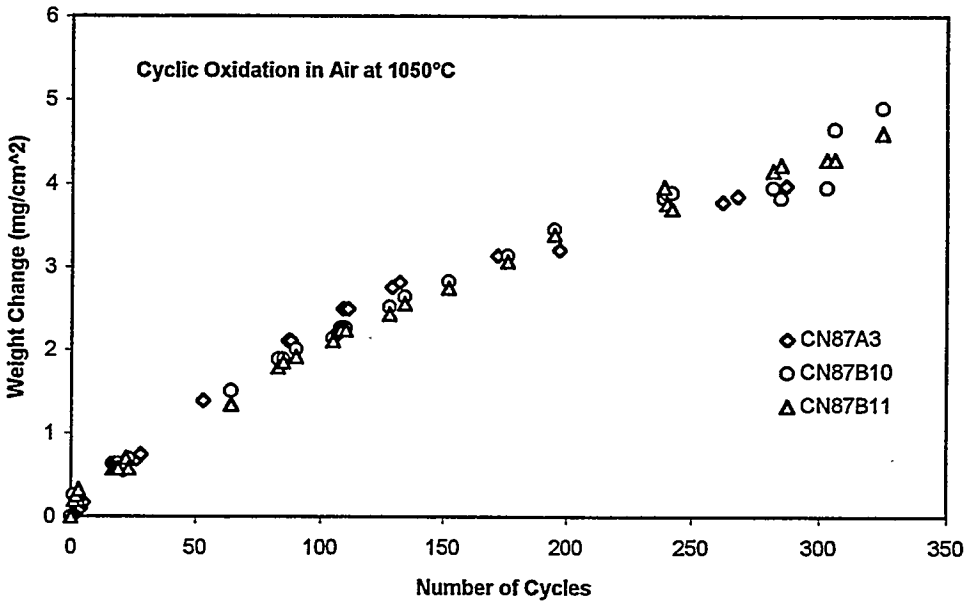

Fig. 4 The cyclic oxidation kinetics of Si-Ge coated CN87 alloy at 1050°C

Figure 7 shows that when fine (20μm) Al powder was used, the Al composition decreased, while the Cr composition increased, with an increase of the particle size of the Cr powder. For some coating runs, chromium carbide layers were produced with a pack using the finest Cr powder. Beneath the carbide, the alloy composition approximated Kanthal. When coarse (-100 mesh) Al powder was used, less extensive variation in Al and Cr concentrations resulted from variation in the particle size of Cr powder, as shown in Fig. 8. Thus the particle sizes of the metals to be used in a codeposition pack cementation process influence importantly the composition of the coating.

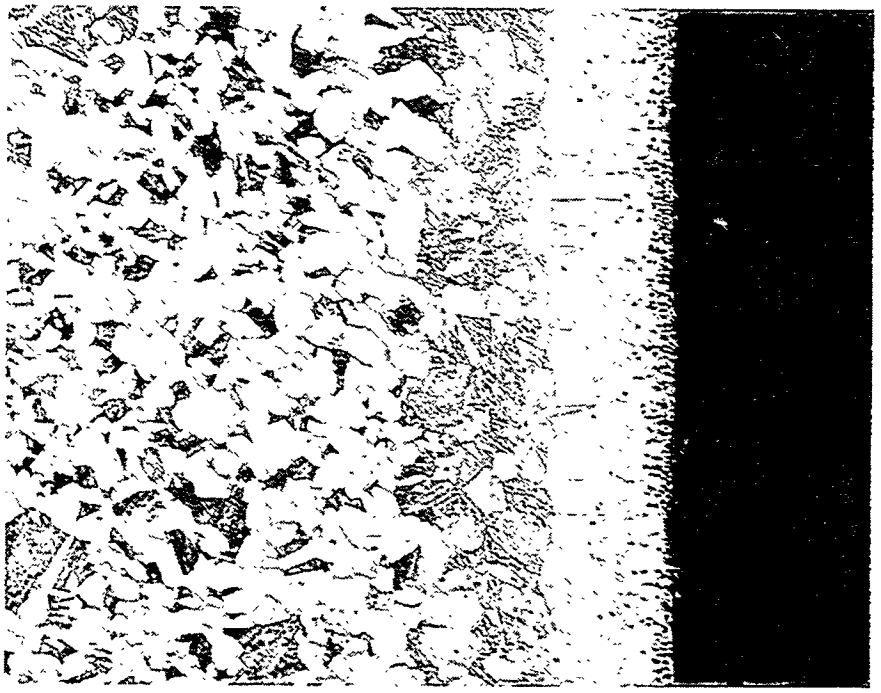

Fig. 5 Photomicrograph of a T11 Substrate with Al and Cr Coating Grown at 920°C for 12 hours Using Pure Cr and Pure Al Powders and Halide Activator (50×)

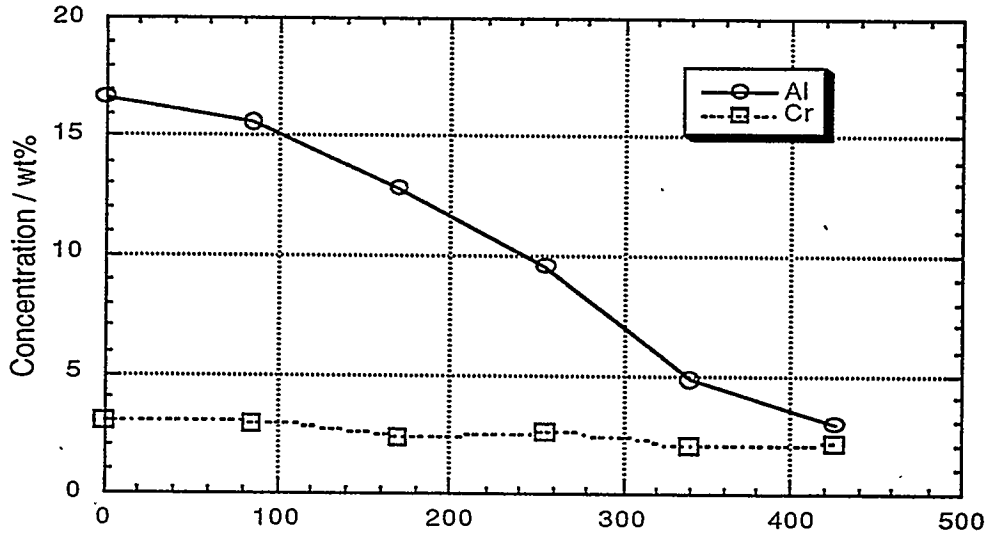

Fig. 6 Concentration Profiles for the Coating on T11 Steel Coated Sequentially at 925°C and 1150°C Using Pure Cr and Al Powders with Halide Activator(s)

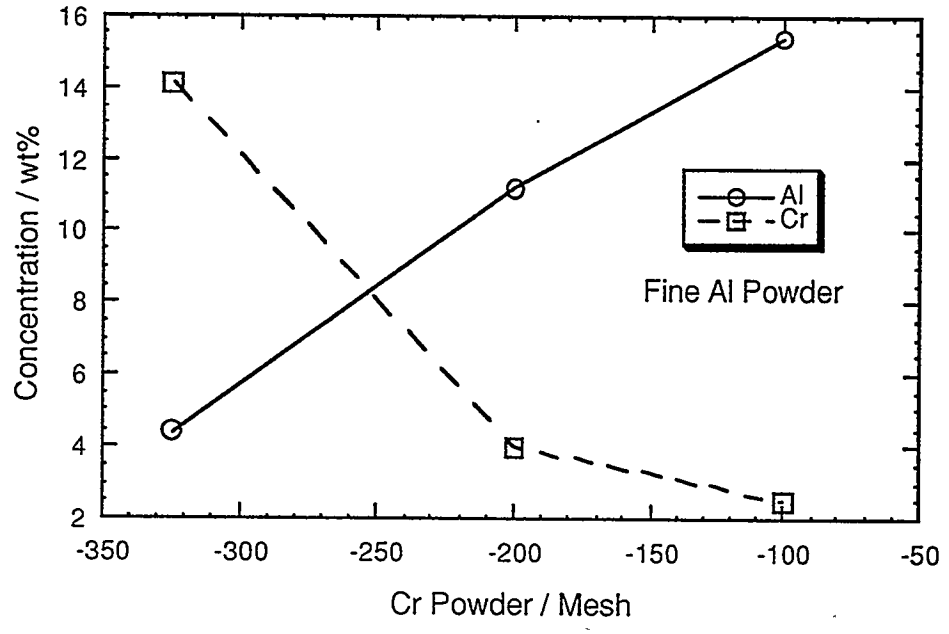

Fig. 7 Surface Compositions of Coatings on T11 Steel Samples vs. Particle Size of Cr Powder in the Pack.

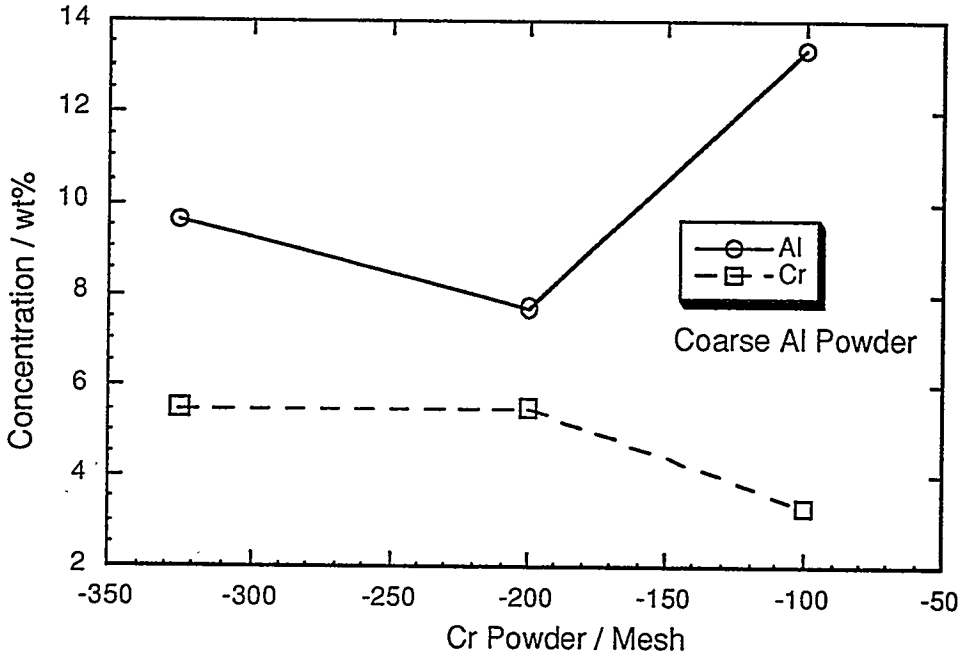

Fig. 8 Surface Compositions of the Coatings on T11 Steel Samples vs. Particle Sizes of Cr Powder in the Pack

CONCLUSIONS

Ge-doped silicide diffusion coatings were developed for the Cr-Nb alloys in a single-step pack cementation process. The morphology and composition of the coating depended both on the composition of the pack, and on the composition and microstructure of the substrate. Higher Ge content in the pack favored $NbSi_2$ formation and suppressed the formation of $CrSi_2$. The thickness of the coating decreased with an increase of Ge in the pack. The Ge-doped silicide coatings minimized the kinetics of cyclic oxidation in air for the Cr-Nb alloys.

The codeposition and diffusion of aluminum and chromium into low alloy steel have been achieved using elemental Al and Cr powders and a two-step pack cementation process. Sequential process treatment at 925°C and 1150°C yields dense and uniform ferrite coatings. The higher content of Al in the coatings was predicted by thermodynamic calculations of equilibrium in the gas phase. The effect of the particle size of the metal powders on the surface composition of the coating has been studied for various combinations of Al and Cr powders.

REFERENCES

1. D. M. Dimiduk, D. B. Miracle, Y-W. Kim and M. G. Mendiratta, ISIJ International, Vol. 31, No. 1, p.1223,1991.

2. C. T. Liu and K. S. Kumar, JOM, May, p. 38, 1993.

3. K. S. Kumar, C. T. Liu, JOM, June, p. 28, 1993.

4. E. P. George, M. Yamaguchi, K. S. Kumar, C. T. Liu, Ann. Rev. Sci., vol. 24, p. 409, 1994.

5. G. Sauthoff, "Intermetallics", VCH Verlagsgesellschaft, New York, 1995.

6. D. L. Anton and D. M. Shah, Materials Science and Engineering, A153, p. 410, 1992.

7. M. Takeyama and C. T. Liu, Materials Science and Engineering, A132, p. 61, 1991.

8. C. T. Liu, J. A. Horton and C. A. Carmichael, Proc. Seventh Ann. Conf. on Fossil Energy Materials, N. C. Cole and R. R. Judkins (Eds.), DOE, p. 297, 1993.

9. P. F. Tortorelli, L. J. Carson and J. H. DeVan, ibid, p. 309, 1993.

10. C. T. Liu, J. A. Horton and C. A. Carmichael Proc. Eighth Ann. Conf. on Fossil Energy Materials, N. C. Cole and R. R. Judkins (Eds.), DOE, p. 377, 1994.

11. P. F. Tortorelli and J. H. DeVan, ibid, p. 391, 1994.

12. C. T. Liu, P. F. Tortorelli, J. A. Horton, D. S. Easton, J. H. Schneibel, L. Heatherly, C. A. Carmichael, M. Howell and J. L. Wright, Proc. Ninth Ann. Conf. on Fossil Energy Materials, N. C. Cole and R. R. Judkins (Eds.), DOE, p. 415, 1995.

13. J. A. Cook, P. K. Liaw and C. T. Liu, ibid, p. 335, 1995.

14. H. J. Grabke and M. Brumm, "Oxidation Behaviour of Chromium Disilicide", Oxidation of High-Temperature Intermetallics, T. Grobstein and J. Doychak (Eds), TMS publisher, p. 245, 1988.

15. W. Douglas, M. L. Fleischer and R. L. Fleischer, Mat. Res. Soc. Symp. Proc. Vol. 213, p. 969, 1991

16. P. G. Cappelli, "Coating Processes", High Temperature Alloys for Gas Turbines, D. Coutsouradis, P. Felix, H. Fischmeister, L. Habraken, Y. Lindblom and M. O. Speidel Eds, Applied Science Publ., London, p. 177, 1978.

17. A. Mueller, G. Wang, R. A. Rapp and E. L. Courtright, J. Electrochem. Soc., 139(5), p.1266, 1992.

18. A. Mueller, G. Wang, R. A. Rapp, E. L. Courtright and T. A. Kircher, Materials Science and Engineering, A155, p. 199, 1992.

19. E. Fitzer, H. Herbst, J. Schlichting, Werkst. Korros. 24, p. 274, 1973.

20. J. Schlichting and S. Neumann, J. Non-Crystalline Solids, 48, p. 185, 1982.

21. B. V. Cockeram, G. Wang and R. A. Rapp, Materials and Corrosion, 46, p. 207, 1995.

22. B. V. Cockeram, G. Wang and R. A. Rapp, Oxid. Met., Vol. 45, Nos.1/2, p. 77, 1996.

23. B. V. Cockeram and R. A. Rapp, Oxid. Met., Vol. 45, Nos.3/4, p. 375, 1996.

24. W. J. Quadakker, T. Malkow and H. Nickel, Proc. 2nd inter. Conf. High Temp. Mat., p. 91, 1995.

25. K. Natesan and R. N. Johnson, Proc. 2nd inter. Conf. High Temp. Mat., p.591, 1995.

26. F. D. Geib and R. A. Rapp, Oxidation of Metals, 40, p. 213, 1993.

27. F. D. Geib and R. A. Rapp, V. A. Ravi and T. S. Srivastsan, Eds., TMS Warrendale, PA, p. 347, 1991.

28. J. D. H. Donnay, "Crystal Data Determinative Tables", Third Edition Vol. 4 Inorganic Compounds, NBS/JCPDS International for Diffraction Data, p. H/R-138, 1972.

29. A. Taylor and B. J. Kagle, "Crystallographic Data on Metal and Alloy Structures", Dover Publications, Inc. New York, p. 143, 1963.